An improved estimate of inorganic iodine emissions from the ocean using a coupled surface microlayer box model

Ryan J. Pound[1], **Lucy V. Brown**[1], **Mat J. Evans**[1,2], and **Lucy J. Carpenter**[1]

[1]Department of Chemistry, Wolfson Atmospheric Chemistry Laboratories,
University of York, York, YO10 5DD, UK
[2]National Centre for Atmospheric Science, University of York, York, YO10 5DD, UK

Correspondence: Ryan J. Pound (ryan.pound@york.ac.uk)

Abstract. Iodine at the ocean's surface impacts climate and health by removing ozone (O_3) from the troposphere both directly via ozone deposition to seawater and indirectly via the formation of iodine gases that are released into the atmosphere. Here we present a new box model of the ocean surface microlayer that couples oceanic O_3 dry deposition to inorganic chemistry to predict inorganic iodine emissions. This model builds on the previous work of Carpenter et al. (2013), improving both chemical and physical processes. This new box model predicts iodide depletion in the top few micrometres of the ocean surface due to rapid chemical loss to ozone competing with replenishment from underlying water. From this box model, we produce parameterized equations for HOI and I_2 emissions, which are implemented into the global chemical transport model GEOS-Chem along with an updated sea surface iodide climatology. Compared to the previous model, inorganic iodine emissions from some tropical waters decrease by as much as half, while higher-latitude emissions increase by a factor of $\gg 10$. With these large local changes, global total inorganic iodine emissions increased by $\sim 49\%$ (2.99 to 4.48 Tg) compared to the previous parameterization. This results in a negligible change in average tropospheric OH ($< 0.2\%$) and tropospheric methane lifetime ($< 0.2\%$). The annual mean tropospheric O_3 burden decreases (-1.5% to 325 Tg); however, higher-latitude surface O_3 concentrations decrease by as much as 20%.

1 Introduction

Iodine in the atmosphere and at the ocean–atmosphere interface is a large sink for tropospheric ozone (O_3). Dry deposition of O_3 to the ocean was thought to account for approximately one-third of the total O_3 loss to dry deposition (Ganzeveld et al., 2009); however, more recent work using more advanced representations of oceanic ozone dry deposition has revised this contribution down to $\sim 15\%$ (Luhar et al., 2018; Pound et al., 2020). At the ocean surface, the reaction between O_3 and iodide (I^-) is thought to represent a significant fraction of this loss (Fairall et al., 2007; Carpenter et al., 2013). Most global models have a simplistic representation of oceanic O_3 dry deposition, which contributes to the uncertainty in tropospheric O_3 (Ganzeveld et al., 2009; Hardacre et al., 2015). Including a more ad-

vanced oceanic dry-deposition scheme that incorporates the chemical loss of O_3 to I^- and the physical processes that control O_3 dry deposition has been shown to improve model comparisons to observations of both oceanic dry-deposition velocity and remote marine surface O_3 concentrations (Luhar et al., 2017, 2018; Pound et al., 2020).

Photochemical cycling of iodine in the atmosphere leads to efficient chemical loss of O_3, perturbs HO_x (Vogt et al., 1999; Alicke et al., 1999; Allan et al., 2000; Bloss et al., 2005), and along with other short-lived halogens emitted from the ocean surface has a substantial indirect impact on climate (Saiz-Lopez et al., 2023). Iodine compounds photolyse to produce atomic iodine (I), which is then rapidly oxidized by O_3 to form iodine oxide (IO). The dominant loss route is $IO + HO_2$ to return to HOI, which upon photolysis leads to a net loss of O_3 (Sommariva et al., 2012; Saiz-

Lopez et al., 2012). The inclusion of iodine emissions and subsequent chemistry into global chemistry transport models decreases tropospheric ozone concentration by 6 %–10 % (Sherwen et al., 2016; Iglesias-Suarez et al., 2020; Pound et al., 2023b), with the largest impact being in the marine boundary layer (MBL) and coastal regions. IO can also impact both HO_x ($OH + HO_2$) and NO_x ($NO + NO_2$) concentrations (Sommariva et al., 2012; Sherwen et al., 2016). However, globally iodine has a small impact on the atmospheric OH concentration. Whilst the reduction in O_3 by iodine reduces the primary chemical production of OH, iodine chemistry increases the conversion of HO_2 to OH, offsetting the reduction in primary production (Sherwen et al., 2016; Pound et al., 2023b).

Organic iodine species have been shown in laboratory experiments as the source of nucleation of new particles in coastal environments (Hoffmann et al., 2001). Recent work has also supported atmospheric iodine playing an important role in particle formation in the MBL, with the impact of iodine on aerosol formation and growth being larger than previously thought (Huang et al., 2022). Combined with more efficient recycling of iodine from aerosol particles (Tham et al., 2021), this could mean that current global chemistry transport models underestimate the role of iodine in aerosol formation and its spatial range of impact.

Recent observations show that approximately 0.7 ppt of reactive iodine species are injected into the stratosphere, largely in the form of longer-lived organic iodine species and particulate iodine (Koenig et al., 2020). This has an important impact on stratospheric O_3, particularly in the tropical lower stratosphere (Saiz-Lopez et al., 2015). Based on these iodine levels reaching the stratosphere, recent model studies have shown that iodine can significantly impact the Antarctic O_3 hole, with iodine's role in modulating stratospheric O_3 likely to increase in relative importance as anthropogenic chlorine and bromine emissions decrease (Cuevas et al., 2022).

I^- in the ocean is formed from the thermodynamically more stable iodate (IO_3^-) via biological reduction processes (Truesdale and Jones, 2000; Chance et al., 2007; Amachi, 2008; Wadley et al., 2020). I^- and IO_3^- combined represent the majority of the total iodine in the ocean. Due to the dependence on biological reduction, I^- concentrations in the ocean could display sensitivity to both seasonal and climate timescales (Carpenter et al., 2021).

The sea surface microlayer (SML) covers the world's oceans to a significant extent, ranging in depth from 1–1000 µm and having distinct chemical and biological properties from underlying waters, and it is the interface between the ocean and atmosphere (Wurl et al., 2011; Cunliffe et al., 2013; Wurl et al., 2017). Following the initial reaction between $O_3 + I^-$ in the top ~ 3 µm of the SML (the reaction–diffusion length), further aqueous chemistry in the SML produces iodinated compounds that can subsequently be emitted into the atmosphere. The largest components of iodine emissions from the ocean surface are the inorganic compounds

HOI and I_2, which are thought to contribute approximately 2 Tg yr^{-1} of iodine to the global atmosphere (Carpenter et al., 2021). An additional 0.6 Tg yr^{-1} of iodine arises from the emission of iodinated hydrocarbons (CH_3I, CH_2I_2, CH_2IBr, and CH_2ICl) (Jones et al., 2010; MacDonald et al., 2014; Prados-Roman et al., 2015).

The O_3 uptake rate by aqueous iodide solutions has been found to be significantly decreased by the addition of surfactants that form a monolayer across the solution and suppress exchange (Rouvière and Ammann, 2010). Laboratory studies of ozonized SML samples found that volatile organic iodine emissions were a negligible fraction of total iodine emissions (Tinel et al., 2020). The addition of organic material has also been found to suppress I_2 emissions from I^- solutions, with this largely being attributed to a decrease in the net transfer of I_2 from the aqueous to gas phase (Reeser and Donaldson, 2011; Shaw and Carpenter, 2013; Tinel et al., 2020). Modelling studies of IO in the Indian Ocean needed to reduce inorganic iodine emissions by 40 % to reasonably match cruise-based observations from the region (Mahajan et al., 2021).

Anthropogenic activity has contributed to increased iodine emissions since preindustrial times (Cuevas et al., 2018; Legrand et al., 2018; Saiz-Lopez et al., 2023), largely due to increased tropospheric O_3 increasing inorganic iodine emissions from the ocean. The increase in anthropogenic emissions from preindustrial to present-day values has also shifted the partitioning of inorganic halogens from reactive to reservoir species (Barrera et al., 2023). Model studies using future climate scenarios forecast a key role of iodine in O_3 destruction through the 21st century (Badia et al., 2021).

Carpenter et al. (2013) created a kinetic box model of the SML to predict inorganic iodine emissions, which were parameterized as functions of surface O_3 concentration, I^- concentration in the ocean, and wind speed. This model predicts exponentially increasing inorganic iodine emissions as wind speed decreases due to an increasing fraction of iodine being emitted to the atmosphere as opposed to being mixed with the underlying water. As such, a minimum wind speed of 5.5 m s^{-1} was applied when implemented in the global chemistry transport model GEOS-Chem (Sherwen et al., 2016). This SML model also does not directly couple the SML chemistry to O_3 dry deposition, and as such it is unable to capture feedback between O_3 deposition, I^- depletion in the SML (Schneider et al., 2020), and the chemical production and emission of inorganic iodine compounds. Finally, the equations provided by Carpenter et al. (2013) did not include a temperature dependence. In reality, there are a host of temperature-dependent processes involved in iodine emissions including the $O_3 + I^-$ reaction (Brown et al., 2024), the diffusivity of O_3 (Johnson and Davis, 1996), and the solubility of HOI and I_2.

Several experiments have measured the rate constant of the $O_3 + I^-$ reaction at a single temperature (Garland et al., 1980; Hu et al., 1995; Liu et al., 2001). A temperature-

dependent rate by Magi et al. (1997) has been used in previous work to model oceanic O_3 dry deposition (Luhar et al., 2017, 2018; Pound et al., 2020) and inorganic iodine emissions (Carpenter et al., 2013). However, the Magi et al. (1997) laboratory study used iodide concentrations of 0.5–3.0 M, which are substantially higher than the typical ocean surface range of 10–100 nM (Chance et al., 2014). At I^- concentrations above 1000 nM, the reaction between O_3 and I^- occurs at the water surface (Moreno et al., 2018). However, with environmental concentrations of I^- at 10–100 nM, the reaction mainly occurs by a different mechanism, within the bulk aqueous phase (Moreno et al., 2018). Ozone uptake experiments under environmentally comparable I^- concentrations also support the aqueous reaction dominating the $O_3 + I^-$ reaction (Schneider et al., 2020; Brown et al., 2024). Recently, Brown et al. (2024) have calculated a new temperature-dependent rate for $O_3 + I^-$ under environmentally comparable iodide concentrations (100–10 000 nM) and an O_3 mixing ratio of 40 ppb at 1 atm. A range of temperatures from 288–303 K were applied, yielding a temperature dependence that can be applied to the interaction of ozone and iodide in the ocean surface. This rate is comparable to other experimental results that did not sample a range of temperatures (Garland et al., 1980; Liu et al., 2001; Hu et al., 1995).

Here we propose a new air–SML–ocean exchange model to couple the processes of oceanic ozone dry deposition to inorganic iodine emissions, which incorporates recent advancements in inorganic iodine chemistry. Section 2 describes the construction of the model and the equations used to describe the physical and chemical components. Sections 3 to 5 diagnose the model's sensitivity to mixing, rate of $O_3 + I^-$ reaction, and salinity and inter-halogen reactions. We then compare this new model to the existing model from Carpenter et al. (2013) (Sect. 7) and experimental results (Sect. 8). Finally, parameterized functions for estimating HOI and I_2 emissions calculated by this coupled ocean–atmosphere exchange model (Sect. 9) are implemented in a global chemical transport model (GEOS-Chem Classic) to give a new estimate for global inorganic iodine emissions and their impact on tropospheric O_3 (Sect. 10).

2 SML box model description

Figure 1 shows a simplified overview of the ocean–atmosphere exchange model described in this paper. Ozone deposition is based on the resistance-in-series scheme and is further described in Sect. 2.1. The SML is composed of many sublayers, defined by their physical, chemical, or biological properties (Soloviev and Lukas, 2014; Carpenter and Nightingale, 2015). This model considers only the top several micrometres of the SML, defined as the reaction–diffusion layer where the rate of chemical loss of O_3 dominates over turbulent transfer (Luhar et al., 2018). This length

scale is dependent on the molecular diffusivity and chemical reactivity of O_3 and given by Eq. (8). The chemistry scheme employed is described in Sect. 2.2. Finally, the mixing of the SML with the atmosphere and the ocean is based on the method described by Cen-Lin and Tzung-May (2013), which is described in Sect. 2.3.1 and 2.3.2, respectively. Table 1 lists all the inputs, outputs, and variables used to calculate the flux of ozone into the SML and the emission of inorganic halogens from the SML.

The model was developed in Python using Cantera as the chemistry solver (Goodwin et al., 2022). The model presented here also uses functions from SciPy (Virtanen et al., 2020), Pandas (Development team, 2020), and NumPy (Harris et al., 2020). Calculations of the salinity- and temperature-dependent unitless Henry's law (H); Schmidt number in the air (S_{ca}); and water (S_{cw}), air-side (k_a), and water-side (k_w) transfer velocities are calculated using the recommended functions from Johnson (2010). The model runs presented here used a physical time step of 1×10^{-4} s and typically reach equilibrium within 4 s.

2.1 Coupled ozone dry deposition

Ozone dry-deposition velocity (v_d) is calculated using the resistance-in-series scheme based on Wesely and Hicks (1977), Eq. (1), this is then used to calculate the flux of ozone into the ocean surface microlayer. Air-side resistances that represent turbulent transport to the surface (r_a) and transport through the atmospheric quasi-laminar sub-layer, which is the air directly above the surface microlayer (r_b), are calculated using Eqs. (2) and (3), respectively (Chang et al., 2004):

$$v_d = \frac{1}{r_a + r_b + r_c}, \tag{1}$$

$$r_a = \frac{u_{10}}{u^{*2}}, \tag{2}$$

$$r_b = \frac{5}{u^*} S_{ca}^{2/3}, \tag{3}$$

where u is the 10 m wind speed with units of m s^{-1}, u^* is the friction velocity with units of m s^{-1}, and S_{ca} is the Schmidt number of O_3 in air and is calculated using the method from Tsilingiris (2008) as recommended by Johnson (2010).

The surface resistance (r_c) captures the chemical and physical processes in the SML that control ozone loss. We employ the two-layer method of Luhar et al. (2018) to calculate r_c, which is shown in Eq. (4).

$$r_c = \frac{1}{\alpha \sqrt{aD}} \left[\frac{\Psi K_1(\xi_\delta) \sinh(\lambda) + K_0(\xi_\delta) \cosh(\lambda)}{\Psi K_1(\xi_\delta) \cosh(\lambda) + K_0(\xi_\delta) \sinh(\lambda)} \right] \tag{4}$$
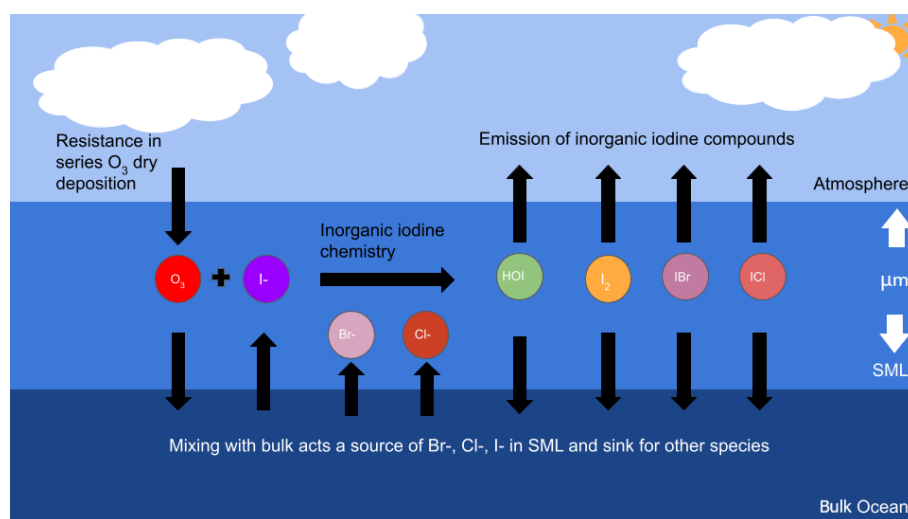
Figure 1. Overview diagram describing the physical arrangement of the ocean surface microlayer and the key chemical species included in the model. The black arrows represent the chemical fluxes and their net direction in this model.

Table 1. All input variables and calculated parameters along with their definitions and dependencies used by the model presented in this work for calculating the dry deposition of O_3 into the SML and fluxes of inorganic halogens to the atmosphere and bulk ocean from the SML.

Variable	Definition	Constant, dependence, or input
T	sea surface temperature	input
u_{10}	10 m wind speed	input
u^*	friction velocity	u_{10}
u_w^*	water-side friction velocity	u_{10}, u^*
C_D	drag coefficient	u_{10}
$[I^-]$	iodide concentration	input
$[O_3]$	ozone concentration	input
C_b	concentration in the bulk ocean	input
S	salinity	input
C_a	concentration in the air	input
κ	von Kármán constant	~ 0.4
S_{cw}	Schmidt number in water	T, S
S_{ca}	Schmidt number in air	T
S_{c600}	Schmidt number of CO_2 at 20 °C	600
r_a	atmospheric resistance to dry deposition	u_{10}, u^*
r_b	quasi-laminar sublayer resistance to dry deposition	u^*, S_{ca}
D	diffusivity of O_3 in water	T
k	second-order rate coefficient of $O_3 + I^-$	T
a	chemical reactivity of $O_3 + I^-$	$[I^-], k$
δ_m	depth of SML reaction–diffusion layer	a, D
α	solubility of O_3 in water	T
r_c	surface resistance to dry deposition	$a, D, \delta_m, \kappa, u_w^*, \alpha$
v_d	dry-deposition velocity	r_a, r_b, r_c
H	unitless Henry's law	T, S
k_a	air-side transfer velocity	S_{ca}, κ, u^*, C_D
k_w	water-side transfer velocity	u_{10}, S_{cw}, S_{c600}
R	surfactant scale factor	0.9
F_a	net flux from the SML to the atmosphere	k_a, H, C_a, C_{sml}
F_b	net flux (molecular transfer) from the SML to the bulk ocean	k_w, R, C_b, C_{sml}
F_r	net flux (surface renewal) from the SML to the bulk ocean	u_{10}, C_b, C_{sml}
C_{sml}	concentration in the SML	F_a, F_b, F_r

The terms ξ_δ, Ψ, and λ are given in Eqs. (5), (6), and (7), respectively:

$$\xi_\delta = \left[\frac{4a}{\kappa u_w^*} \left(\delta_m + \frac{D}{\kappa u_w^*} \right) \right]^{\frac{1}{2}}, \tag{5}$$

$$\Psi = \left[1 + \left(\frac{\kappa u_w^* \delta_m}{D} \right) \right]^{\frac{1}{2}}, \tag{6}$$

$$\lambda = \delta_m \sqrt{\frac{a}{D}}, \tag{7}$$

where u_w^* (m s^{-1}) is the water-side friction velocity and δ_m is the thickness of the reaction–diffusion layer of the sea surface microlayer (m) calculated using Eq. (8) (Luhar et al., 2017). K_0 and K_1 are modified Bessel functions of the second kind with order 0 and 1, respectively, and κ is the von Kármán constant (≈ 0.4); a is the chemical reactivity of O$_3$ with I$^-$ (defined in Eq. 9). It uses the second-order rate coefficient (k) from either Magi et al. (1997) or Brown et al. (2024) with units of M^{-1} s^{-1}. The diffusivity O$_3$ in the SML (D, m^2 s^{-1}) is from Johnson and Davis (1996) and shown in Eq. (10). This calculation of D does not account for the impact of organics (particularly surfactants), which will impact the transfer of O$_3$ into the SML; this model is currently limited to inorganic chemistry, and the limitations of this are discussed further in Sect. 11. Here, α is the dimensionless solubility of O$_3$ from Morris (1988) shown in Eq. (11).

$$\delta_m = \sqrt{\frac{D}{a}} \tag{8}$$

$$a = k \left[I^- \right] \tag{9}$$

$$D = 1.1 \times 10^{-6} \exp\left(\frac{-1896}{T} \right) \tag{10}$$

$$\alpha = 10^{-0.25 - 0.013(T - 273.16)}. \tag{11}$$

The dry-deposition velocity (v_d) is coupled to the SML chemistry via the I$^-$ concentration and is recalculated as the model advances in time towards equilibrium.

2.2 Chemistry

The aqueous inorganic halogen chemistry scheme used in this model is shown in Table 2. Here we employ an extended version of the iodine chemistry scheme used by Carpenter et al. (2013) and similar to that of Schneider et al. (2023) with the addition of further inter-halogen reactions involving bromine and chlorine species. A further difference between this chemistry scheme and that of Carpenter et al. (2021) is that we explicitly include the reaction step of O$_3$ + I$^-$ producing IO$^-$ (Reaction R1a) rather than HOI directly, alongside its subsequent conversion to HOI (Reaction R7). This has little impact on the total simulated inorganic iodine emissions as IO$^-$ quickly reacts to form HOI at ocean pH, but it presents a more complete representation of the chemistry.
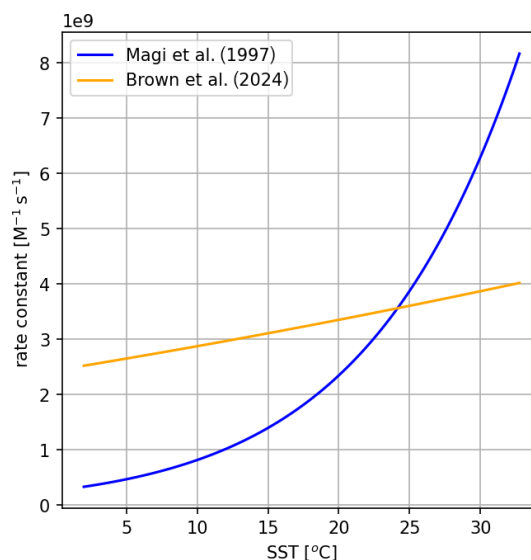

Figure 2. Comparison of the two published temperature-dependent rate coefficients from Magi et al. (1997) (blue) and Brown et al. (2024) (orange).

To explore the sensitivity of total iodine emissions to the rate coefficient of the O$_3$ + I$^-$ reaction, two different forms of the temperature-dependent rate coefficient are used. The first of these (reaction R1a from Table 2) uses the rate published by Magi et al. (1997), which is also the rate used by Carpenter et al. (2013) in their model. The second rate (Reaction R1b from Table 2) is the more recent temperature-dependent rate from Brown et al. (2024), which has a much weaker temperature dependence than that of Magi et al. (1997). The different temperature dependencies of these two rates are shown in Fig. 2.

2.3 Mixing processes

2.3.1 Emissions of inorganic iodine

The net flux of a species from the SML into the atmosphere (F_a) is calculated from the concentration in the SML (C_{sml}) and the concentration in the atmosphere (C_a, Eq. 12). Atmospheric fluxes are calculated for HOI, I$_2$, IBr, ICl, HOCl, HOBr, Br$_2$, Cl$_2$, and BrCl. HOI and I$_2$ have the largest fluxes, with the other species emitted in negligible amounts due to their high solubility and relatively low concentrations in the SML.

$$F_a = k_a (H \cdot C_{sml} - C_a) \tag{12}$$

k_a is calculated following the recommendation from Johnson (2010) using Eq. (13):

$$k_a = + \frac{u_*}{13.3 S_{ca}^{0.5} + C_D^{-0.5} - 5 + \frac{\ln(S_{ca})}{2\kappa}}, \tag{13}$$

Table 2. All reactions included in the chemistry scheme of this SML model with forward and reverse rate constants (where applicable) and accompanying references. Numbered reactions with a and b denote different rates explored in the sensitivity analysis conducted in this paper. The (1) is used to indicate $A = 1.44 \times 10^{22}\,\mathrm{M^{-1}\,s^{-1}}$ and $Ea = 73.08\,\mathrm{kJ\,mol^{-1}}$. The (2) is used to indicate $A = 2.6 \times 10^{11}\,\mathrm{M^{-1}\,s^{-1}}$ and $Ea = 10.6\,\mathrm{kJ\,mol^{-1}}$. The (3) is used to indicate the assumed reaction based on theoretical calculation.

Number	Reaction	Forward rate	Reverse rate	Reference
R1a	$O_3 + I^- \rightarrow IO^-$	(1)	n/a	Magi et al. (1997)
R1b		(2)	n/a	Brown et al. (2024)
R2	$I_2 \leftrightarrow I_2OH^- + H^+$	3.2	2.0×10^{10}	Lengyel et al. (1993)
R3	$I_2OH^- \leftrightarrow HOI + I^-$	1.34×10^6	4.0×10^8	Lengyel et al. (1993)
R4	$I^- + I_2 \leftrightarrow I_3^-$	6.2×10^9	8.9×10^6	Lengyel et al. (1993)
R5	$HOI + HOI \leftrightarrow H^+ + I^- + HIO_2$	25	2.0×10^{10}	Paquette (1989)
R6	$I_2 + OH^- \leftrightarrow HOI + I^-$	7.0×10^4	2.1×10^3	Sebők-Nagy and Körtvélyesi (2004)
R7	$HOI \leftrightarrow IO^- + H^+$	0.1	1×10^{10}	Paquette (1989)
R8	$HOI + IO^- \rightarrow HIO_2 + I^-$	15	n/a	Bichsel and von Gunten (2000)
R9	$HIO_2 + HOI \leftrightarrow IO_3^- + I^- +, 2H^+$	240	1.2×10^3	Paquette (1989)
R10	$H_2OI^+ \leftrightarrow HOI + H^+$	9.0×10^8	2.0×10^{10}	Lengyel et al. (1993)
R11	$I_2 + H_2O \leftrightarrow H_2OI^+ + I^-$	0.12	1.0×10^{10}	Lengyel et al. (1993)
R12	$HOI + Br^- + H^+ \leftrightarrow IBr$	4.1×10^{12}	8.0×10^5	De Barros Faria et al. (1993)
R13	$HOI + Cl^- + H^+ \leftrightarrow ICl$	2.9×10^{10}	2.4×10^6	Wang et al. (1989)
R14	$I_2 + Br^- \leftrightarrow I^- + IBr$	4.64×10^3	2.0×10^9	De Barros Faria et al. (1993)
R15a	$I_2 + Cl^- \leftrightarrow I_2Cl^-$	8.33×10^4	5.0×10^4	Kumar et al. (1986)
R15b		8.33×10^4	5.0×10^3	Schneider et al. (2023)
R16	$ICl_2^- \leftrightarrow ICl + Cl^-$	1.1×10^9	1.5	Kumar et al. (1986)
R17	$I^- + ICl \leftrightarrow I_2Cl^-$	1.1×10^9	1.5	Kumar et al. (1986)
R18[3]	$ICl_2^- + I^- \rightarrow I_2Cl^- + Cl^-$	1.0×10^6	n/a	Kumar et al. (1986)
R19	$HOCl + I^- + H^+ \rightarrow ICl + H_2O$	3.5×10^{11}	n/a	Nagy et al. (1988)
R20	$HOI + HOCl \rightarrow HIO_2 + Cl^- + H^+$	5.0×10^5	n/a	Citri and Epstein (1988)
R21	$HIO_2 + HOCl \rightarrow IO_3^- + Cl^- + 2H^+$	1.5×10^3	n/a	Lengyel et al. (1996)
R22	$Cl^- + O_3 + H^+ \rightarrow HOCl + O_2$	1.1×10^5	n/a	Levanov et al. (2019)
R23	$Br^- + O_3 + H^+ \rightarrow HOBr + O_2$	11.7	n/a	Haag and Hoigné (1983)
R24	$HOBr + Cl^- + H^+ \rightarrow BrCl + H_2O$	5.6×10^9	n/a	Wang et al. (1994)
R25	$HOBr + Br^- + H^+ \rightarrow Br_2 + H_2O$	1.6×10^{10}	n/a	Beckwith et al. (1996)
R26	$HOCl + Cl^- + H^+ \rightarrow Cl_2 + H_2O$	2.2×10^4	n/a	Wang and Margerum (1994)
R27	$HOCl + Br^- + H^+ \rightarrow BrCl + H_2O$	1.3×10^6	n/a	Kumar and Margerum (1987)
R28	$BrCl + H_2O \rightarrow HOBr + Cl^- + H^+$	1.0×10^5	n/a	Wang et al. (1994)
R29	$Br_2 + H_2O \rightarrow HOBr + Br^- + H^+$	97	n/a	Beckwith et al. (1996)
R30	$Cl_2 + H_2O \rightarrow HOCl + Cl^- + H^+$	22	n/a	Wang and Margerum (1994)
R31[3]	$BrCl + Br^- \rightarrow Br_2Cl^-$	5.0×10^9	n/a	Michalowski et al. (2000)
R32[3]	$Br_2 + Cl^- \rightarrow Br_2Cl^-$	5.0×10^9	n/a	Michalowski et al. (2000)
R33[3]	$BrCl + Cl^- \rightarrow BrCl_2^-$	5.0×10^9	n/a	Michalowski et al. (2000)
R34	$Br_2Cl^- \rightarrow Br_2 + Cl^-$	3.9×10^9	n/a	Wang et al. (1994)
R35	$Br_2Cl^- \rightarrow BrCl + Br^-$	2.8×10^8	n/a	Wang et al. (1994)
R36	$BrCl_2^- \rightarrow Cl_2 + Br^-$	690	n/a	Wang et al. (1994)

n/a: not applicable.

where u_* is the friction velocity ($\mathrm{m\,s^{-1}}$) and C_D is the drag coefficient ($\mathrm{m\,s^{-1}}$) from Smith (1980)

$$10^3 C_D = 0.61 + 0.063 u_{10}. \tag{14}$$

2.3.2 Ocean mixing with SML

This model employs SML concentrations mixing with the bulk ocean concentration (C_b) on two timescales and follows the approach used by Cen-Lin and Tzung-May (2013). The first mixing process, molecular transfer, occurs on the order
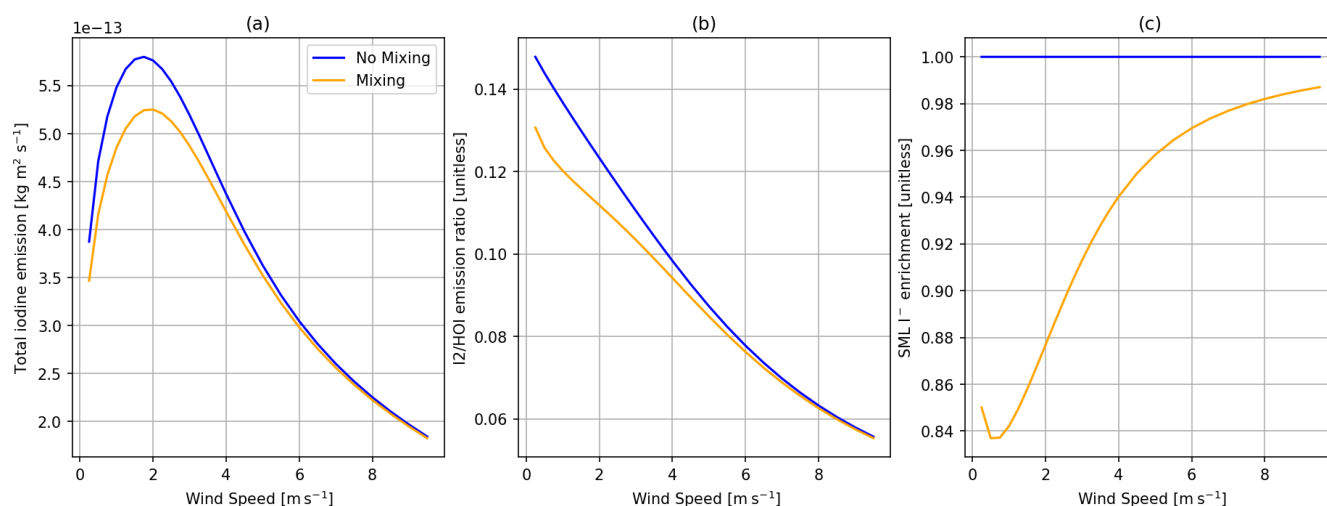
Figure 3. Comparisons of the SML model predictions with no mixing of I^- (100 nM in both the SML and bulk layers) (blue) and mixing of I^- from the bulk layer and varying in the SML (orange). **(a)** Total inorganic iodine emission ($HOI + I_2 + IBr + ICl$) vs. wind speed, **(b)** the ratio of I_2 / HOI emission vs. wind speed, and **(c)** SML I^- enrichment (SML concentration/bulk concentration) vs. wind speed. All calculations are performed at 30 ppb of atmospheric O_3, 100 nM I^- concentration in bulk water, and 285 K sea surface temperature (SST).

of 0.1–1 s and is given by Eq. (15).

$$F_b = Rk_w (C_b - C_{sml}), \quad (15)$$

where R accounts for the effects of surfactants suppressing the transport between the SML and bulk ocean. A value of 0.9 is used in this study to represent the open ocean (Goldman et al., 1988; Frew et al., 1990; Cen-Lin and Tzung-May, 2013). k_w is calculated using Eq. (16), which follows the recommendations of Johnson (2010) in using the Nightingale et al. (2000) approach. u_{10} is the 10 m wind speed, S_{cw} is the Schmidt number of the gas in water, and S_{c600} Schmidt number of CO_2 at 20 °C.

$$k_w = \left(0.222u_{10}^2 + 0.333u_{10}\right) \left(\frac{S_{cw}}{S_{c600}}\right)^{0.5} \quad (16)$$

The second mixing process is surface renewal, representative of larger-scale eddy mixing, and is given by Eq. (17). It is a significantly slower process than the mixing described above and is typically on the order of minutes or longer but has been included for completeness. Surface renewal and the suppression of transfer velocity by surfactants (R) are new developments in this model compared to Carpenter et al. (2013).

$$F_r = \left(3.42 \times 10^{-3}u_{10} + 2.7 \times 10^{-3}\right)(C_b - C_{sml}) \quad (17)$$

Fluxes for mixing between the SML and bulk ocean are calculated for HOI, I_2, O_3, IBr, ICl, IO_3^-, HOBr, HOCl, Br_2, Cl_2, BrCl, I^-, Br^-, and Cl^-. The mixing processes described here are only representative of passive diffusion and do not take into account any electrostatic effects. Solutions with ions have been found to have stronger electric fields at the air–water interface than within the bulk due to charge separation and this can contribute to an increased concentration

of ions and enhanced reaction rates (Xiong et al., 2020; Hao et al., 2022). However, given that the fast turbulent-driven mixing of the SML with the bulk water and the chemical depletion of I^- within the SML occur on timescales of seconds or less under typical conditions, we consider additional effects that could impact the enhancement or depletion of I^- within the SML as likely being secondary. The control of I^- in the SML by the equilibrium of chemical and physical processes represents a significant difference between this work and that of Carpenter et al. (2013), where it was prescribed as a constant. The impact of this difference is explored in Sect. 3.

The concentration of I^- is set based on the conditions being studied by the model. Unless otherwise stated, the sensitivity studies presented here use a concentration of 100 nM. Br^- concentrations are set at 0.86 mM and Cl^- at 0.55 M to replicate typical ocean salinity. The oceanic concentration of IO_3^- is set at 200 nM (Chance et al., 2020). All other species are assumed to have zero bulk oceanic concentrations. H^+ and OH^- are not subject to mixing and are manually set at each time step to maintain a constant pH of 8.

3 Depletion of SML iodide

One difference between this and previous work is the model prediction of depletion of I^- in the SML at low wind speeds (Figs. 3 and 4) due to its reaction with O_3. This is a direct consequence of the slow replenishment of I^- in the SML from mixing with bulk water rather than being a fixed quantity as in previous models. Depletion of I^- has been previously detected experimentally in artificial seawater (Schneider et al., 2023). The effect of this depletion on total inor-

ganic iodine emission and the composition of that emission is shown in Fig. 3. To a lesser extent, depletion of I^- is also greater at higher sea surface temperature (SST), as shown in Fig. 4; this is entirely driven by the temperature dependence of the $O_3 + I^-$ reaction.

The depletion of I^- accounts for roughly an 11 % reduction in total inorganic iodine emissions at $2\,m\,s^{-1}$ wind speed, 285 K, 30 ppb O_3, and 100 nM of I^- in bulk water (Fig. 3). The reduction in SML I^- concentration also reduces O_3 dry-deposition velocity by 15 % under the same conditions.

4 Sensitivity to the temperature dependence of the I^- + O_3 reaction

Here we compare two temperature-dependent rate constants for the $I^- + O_3$ reaction. The first of these is that of Magi et al. (1997), which has been used in the previous model of Carpenter et al. (2013). We compare this to the more recent rate from Brown et al. (2024), which was derived from experiments conducted at I^- concentrations of ~ 100–10 000 nM. The difference in the temperature dependence of total inorganic iodine emission is shown in Fig. 5. The newer rate constant results in substantially higher total inorganic iodine emissions at low SST. At 285 K, total inorganic iodine emissions increase by $\sim 130\,\%$ when using the rate coefficient from Brown et al. (2024) compared to Magi et al. (1997) (Fig. 5a), while O_3 dry-deposition velocity increases by 36 %. Both increases are offset by I^- enrichment decreasing from $\sim 96\,\%$ to $\sim 90\,\%$ at the same temperature (Fig. 5c). Increased depletion of I^- in the SML also results in the production pathways of I_2 from HOI becoming less competitive, resulting in the amount of I_2 emission relative to HOI decreasing (Fig. 5b). At higher temperatures (above $\sim 25\,°C$, Fig. 2), the Brown et al. (2024) rate is slower than that of Magi et al. (1997), resulting in decreased HOI production; however, this is somewhat offset by the sensitivity of the model to the reaction–diffusion length, which is dependent on this rate and is explored in Sect. 6. All subsequent experiments using the box model use the Brown et al. (2024) rate due to it better reflecting the $O_3 + I^-$ reaction under oceanic conditions.

5 I_2 emission salinity sensitivity

The experimental work of MacDonald et al. (2014) found a strong increase in I_2 emission at higher salinity, which was replicated in their accompanying model results. We also predict a positive salinity dependence on I_2 emissions in our base model (Fig. 6). The increase in I_2 emissions is partly from the additional chemical pathway to produce I_2 via ICl as concluded by MacDonald et al. (2014) (Reactions R13, R15 and R17 in Table 2). Additionally, the changes in solubility (due to salinity due to the salinity dependence of H and

S_{cw}, salting out effect) increase the total iodine emissions, as shown by the difference between the green and yellow lines in Fig. 6, where the chloride concentration was set to achieve a salinity of 35 PSU but the chlorine chemistry was removed from the chemical mechanism. The increase in total iodine emissions from the increase in I_2 emission has a negligible impact on HOI emissions, as HOI is in excess in the SML (Carpenter et al., 2013).

The largest increase in I_2 emission with the addition of salinity is observed in low-turbulence conditions (low wind speed, Fig. 6b); here the effects on solubility have a larger effect than the additional chemical pathway to I_2 production provided by Cl^-. Under the conditions used in this study, I_2 emissions are increased by $\sim 150\,\%$ with the addition of Cl^-. However, this is less than the 250 % increase observed by MacDonald et al. (2014). Differences between experimental results and this model are discussed further in Sect. 8. Figure 6 shows that, similar to chloride, increasing bromide increases total I_2 production. This increase is the result of the additional pathway via IBr to produce I_2 (Reactions R12 and R14 in Table 2).

In contrast to these results, more recent work from Tinel et al. (2020) and Schneider et al. (2023) did not find an increase in I_2 emissions from increasing Cl^-. I_2 emissions were instead suppressed in saline samples compared to purely iodide solutions. Schneider et al. (2023) found that their results could be replicated by shifting the equilibrium for Reaction R15a in Table 2 to favour I_2Cl^- over I_2 (Reaction R15b in Table 2). The result of implementing that change to the equilibrium in this model is shown in Fig. 7. The rate of I_2 production through the additional chemical pathway provided by ICl is reduced, and iodine emissions decrease by up to 5 %. Depletion of I^- is unaffected.

6 Inorganic iodine emission sensitivity to reaction–diffusion layer depth

Here we explore the sensitivity of predicted iodine emission fluxes to the depth of the reaction–diffusion layer (δ_m). The values of δ_m calculated are typically between 2.2–2.9 µm for the conditions shown in Figs. 8 and 9 (using Eq. 8 and the Brown et al., 2024, rate constant). δ_m is directly dependent on SML temperature via O_3 diffusivity D and the chemical reactivity a, with a also giving δ_m a direct dependence on $[I^-]$. There is an indirect dependence between δ_m and wind speed due to the depletion of iodide in the SML that increases in low-turbulence conditions. Under conditions with higher turbulence ($> 3\,m\,s^{-1}$), larger δ_m values increase total inorganic iodine emissions. However, under less well-mixed conditions, the coupling of mixing and the availability of I^- in the SML creates a more complex relationship between total inorganic iodine emission and δ_m. Further improvements to model predictions of total inorganic iodine emissions are therefore dependent on our understanding of the reaction–
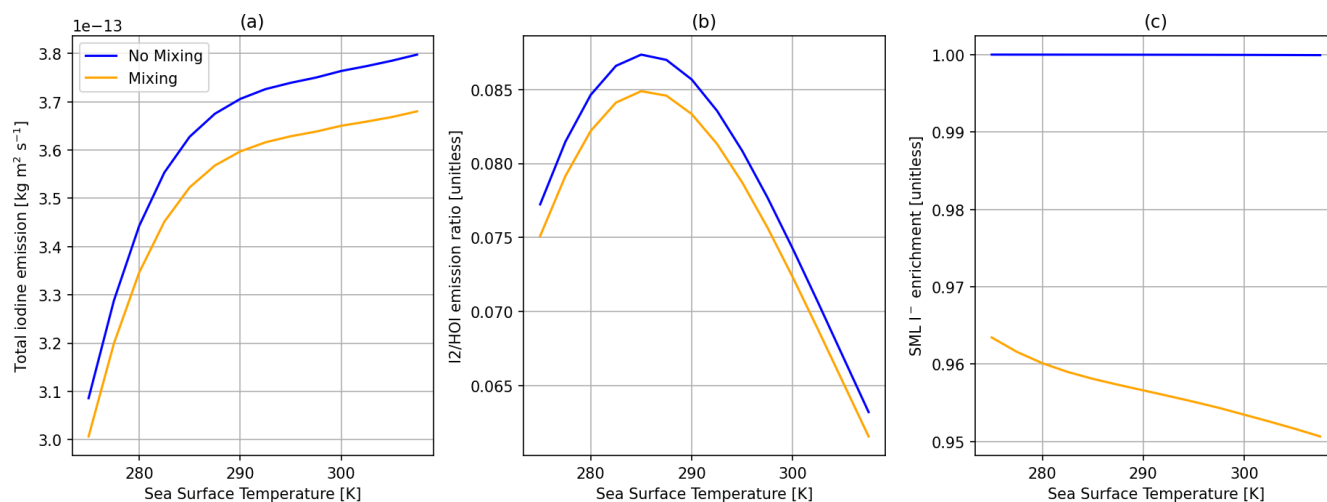
Figure 4. Comparisons of the SML model predictions with no mixing of I^- (100 nM in both the SML and bulk layers) (blue) and mixing of I^- from the bulk layer and varying concentration in the SML (orange). **(a)** Total inorganic iodine emission ($HOI + I_2 + IBr + ICl$) vs. SST. **(b)** The ratio of I_2 / HOI emission vs. SST. **(c)** SML I^- enrichment (SML concentration/bulk concentration) vs. SST. All calculations are performed at 30 ppb of atmospheric O_3, 100 nM I^- concentration in bulk water, and 5 m s^{-1} wind speed.
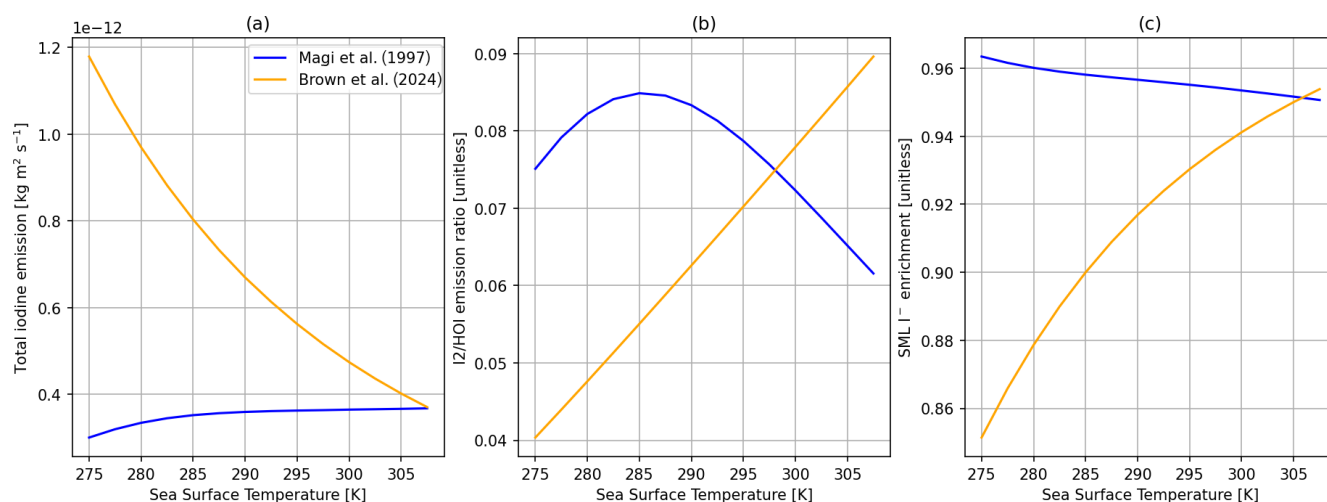
Figure 5. Comparisons of the SML model with the $I^- + O_3$ rate reported by Magi et al. (1997) (blue) and Brown et al. (2024) (orange). **(a)** Total inorganic iodine emission vs. SST. **(b)** The ratio of I_2 / HOI emission vs. SST. **(c)** SML I^- enrichment (SML concentration/bulk concentration) vs. SST. All calculations are performed at 30 ppb of atmospheric O_3, 5 m s^{-1} wind speed, and 100 nM I^- concentration in bulk water.

diffusion length and uncertainties in both D and the rate of $O_3 + I^-$ (Reaction R1).

7 Comparisons to existing model

Figure 10 compares the total iodine emissions predicted in this work to that of Carpenter et al. (2013) across wind speed, iodide, ozone, and temperature ranges. The new model uses the $O_3 + I^-$ rate from Brown et al. (2024) and the updated equilibrium of Reaction R15b from Schneider et al. (2023). Temperature dependence was not included in the Carpenter et al. (2013) equations. Two versions of the Carpenter et al.

(2013) model are used in the wind speed comparison. The first is the equations as presented (solid black line), while the second has a minimum wind speed of 5.5 m s^{-1} applied (dashed black line, as used in the global modelling study of Sherwen et al. (2016)). For total iodine emission at the highest wind speeds, the new model tends towards the old model. This is due to the efficient mixing at these higher wind speeds resulting in negligible I^- depletion in the SML, and it thus more closely resembles the old model, which included a constant I^- concentration in the SML. As wind speed decreases, the two models diverge in their prediction of total iodine emission, with the new model predicting less emis-
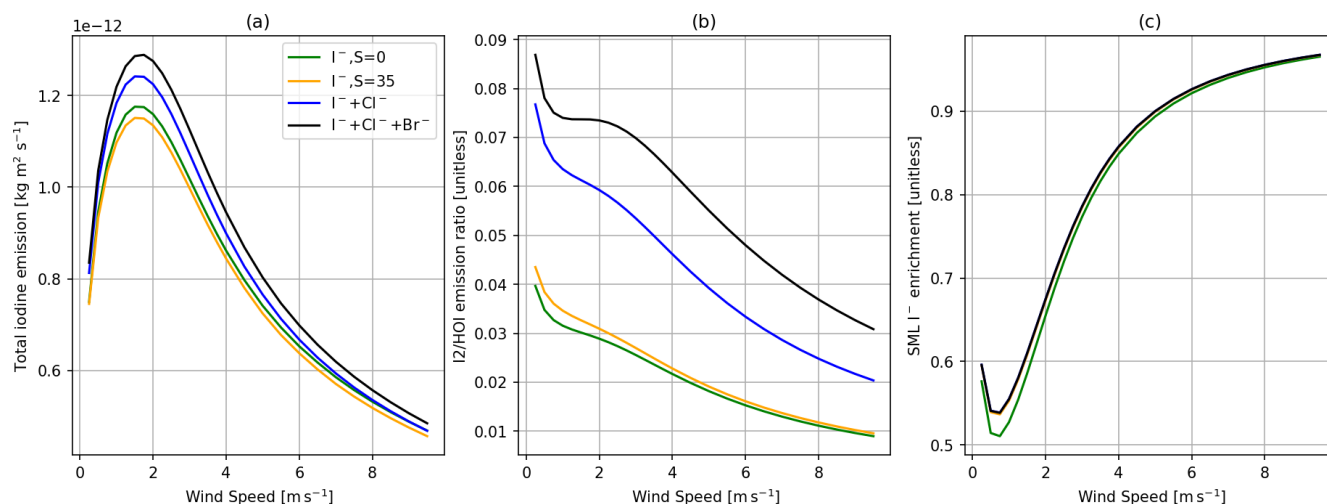
Figure 6. Comparisons of the SML model with only iodine chemistry (green), only iodine chemistry but with a salinity of 35 PSU (orange), iodine and chlorine chemistry (blue), and with the full chemistry scheme present (iodine, bromine, and chlorine chemistry, black). Panel **(a)** shows total inorganic iodine emission vs. wind speed, panel **(b)** shows the ratio of I_2 / HOI emission vs. wind speed, and panel **(c)** shows SML I^- enrichment (SML concentration/bulk concentration) vs. wind speed. All calculations are performed at 30 ppb of atmospheric O_3, 285 K SST, and 100 nM I^- concentration in bulk water.
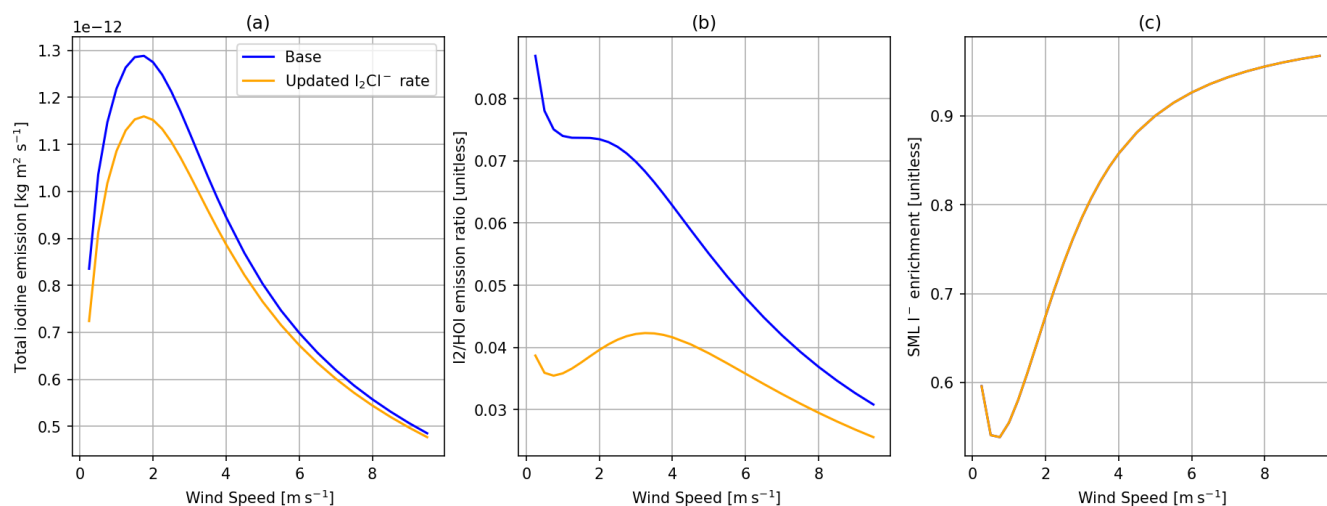
Figure 7. Comparisons of the SML model with $I^- + O_3$ rate using the standard chemistry scheme (blue) and the updated equilibrium from Schneider et al. (2023) (orange). Panel **(a)** shows total inorganic iodine emission vs. wind speed, panel **(b)** shows the ratio of I_2 / HOI emission vs. wind speed, and panel **(c)** shows SML I^- enrichment (SML concentration/bulk concentration) vs. wind speed, with all calculations using 30 ppbv of atmospheric O_3, 285 K SST, and 100 nM I^-.

sion flux than the capped and uncapped (Carpenter et al., 2013) model. This decrease is most notable at very low wind speeds where the new model tends towards no iodine emission as wind speed tends towards zero, rather than the Carpenter et al. (2013) model where total iodine emissions exponentially increase as wind speed tends to zero.

Carpenter et al. (2013) found a simple multiplicative and approximately linear relationship between O_3 concentration and total iodine emission. The slightly dampened relationship between O_3 and total iodine emission in this model is

likely because higher O_3 concentration causes a greater depleting effect on SML I^- concentration, reducing total iodine emission. The new model predicts a similar trend of I^- dependence of total iodine emission to Carpenter et al. (2013). Additionally, the new model predicts that I_2 contributes a larger percentage of total iodine emissions, despite the change made to the chemistry scheme to reflect lower I_2 emissions under oceanic salinity. This difference is likely due to a reduced HOI emission flux from the SML, resulting in
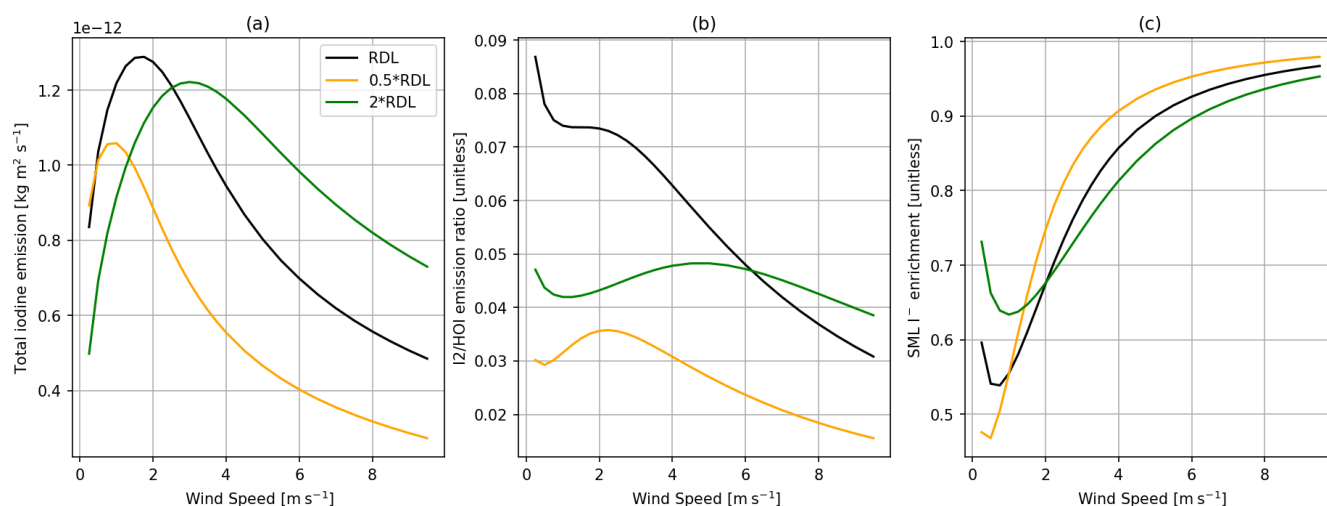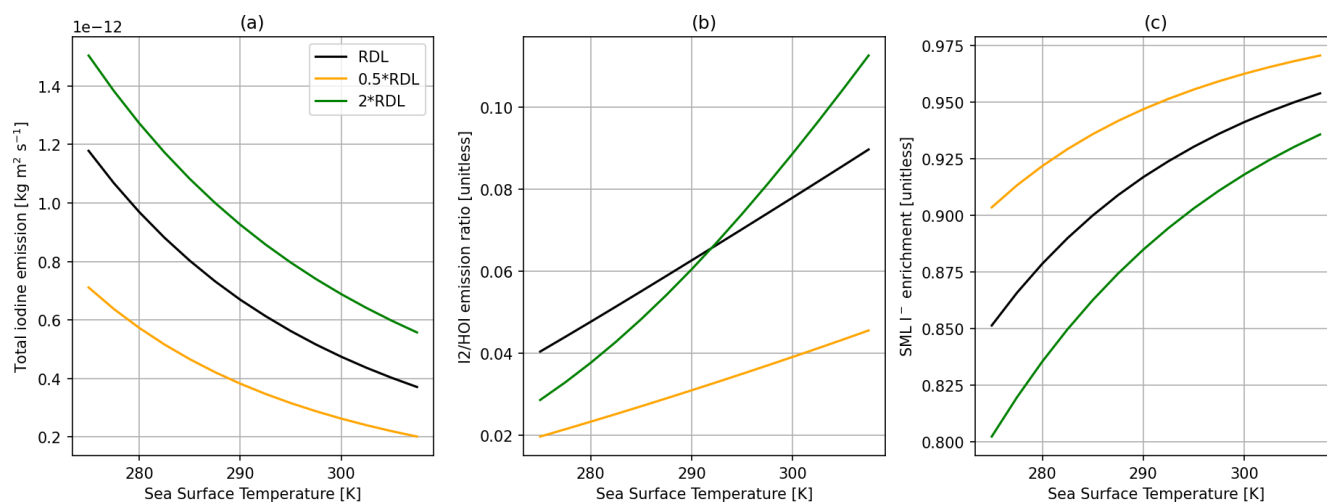
Figure 8. Comparisons of the SML model with the depth of the model being half (orange) and twice (green) the reaction–diffusive length (RDL) and the base model using a single reaction–diffusion length (black). Panel **(a)** shows total inorganic iodine emission vs. wind speed, panel **(b)** shows the ratio of I_2 / HOI emission vs. wind speed, and panel **(c)** shows SML I^- enrichment (SML concentration/bulk concentration) vs. wind speed, with all calculations using 30 ppbv of atmospheric O_3, 285 K wind speed, and 100 nM I^-.

Figure 9. Comparisons of the SML model with the depth of the model being half (orange) and twice (green) the reaction–diffusive length (RDL) and the base model using a single reaction–diffusion length (black). Panel **(a)** shows total inorganic iodine emission vs. SST, panel **(b)** shows the ratio of I_2 / HOI emission vs. SST, and panel **(c)** shows SML I^- enrichment (SML concentration/bulk concentration) vs. SST, with all calculations using 30 ppbv of atmospheric O_3, 5 m s^{-1} wind speed, and 100 nM I^-.

more of the aqueous HOI remaining in the SML, which can subsequently produce more I_2.

8 Comparisons to experimental data

Table 3 compares published experimental results for I_2 fluxes to predictions from this model under conditions that match those used in the various experimental studies. One limitation in this comparison is replicating the water-side turbulence due to stirring (or not) of the aqueous solution and from the gas flow over the solution. Experimental setups which do

not stir the solution have very different dynamics to the ocean surface, which this model has been designed to replicate. Additionally, some experimental results use O_3 and I^- concentrations significantly higher than typical environmental conditions due to measurement instrument sensitivity (Table 3). The model significantly underestimates experimental results where the solutions were not stirred, possibly due to a high depletion of surface iodide under such conditions, which reduces the potential for gaseous iodine emissions (Schneider et al., 2023). For stirred experiments, however, the model predicts a similar range of I_2 emissions as the experiments.
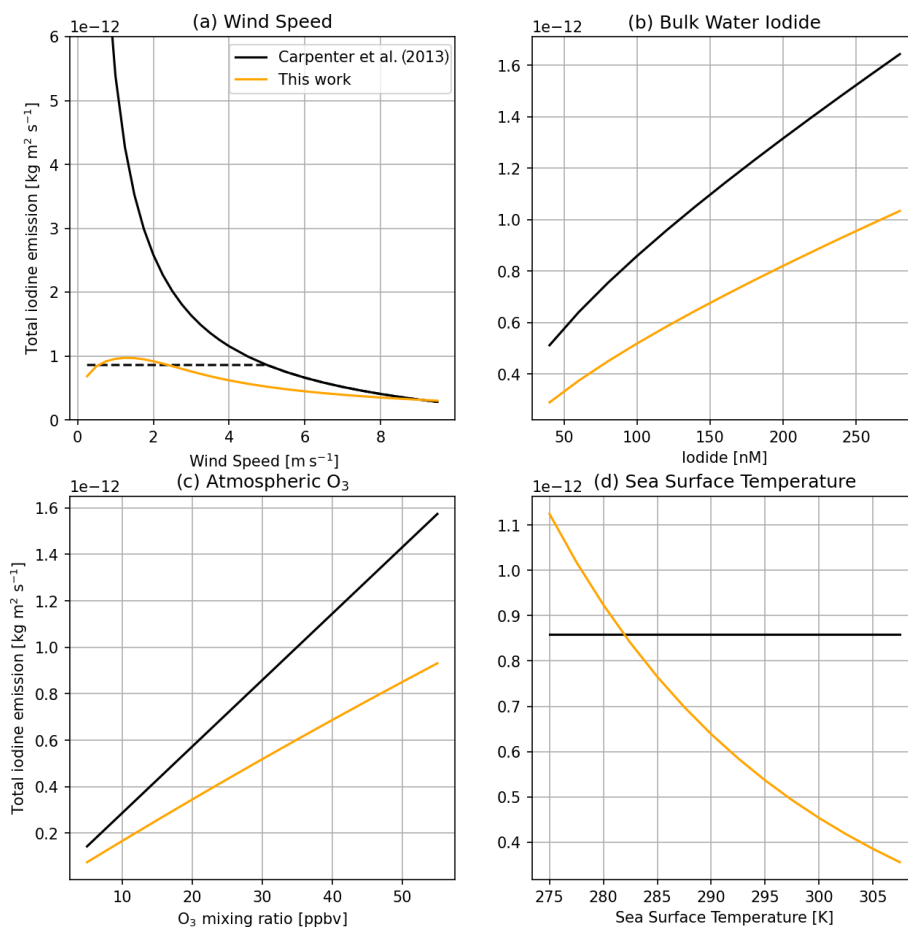
Figure 10. Comparison between total iodine emissions from this work and the model as implemented by Carpenter et al. (2013) across a range of wind speeds **(a)** (both with (dashed black line) and without (solid black line) a minimum wind speed of 5.5 m $^{-1}$), bulk water iodide concentrations **(b)**, atmospheric O_3 mixing ratios **(c)**, and sea surface temperatures **(d)**.

Table 3. Comparison of I_2 emissions from published experimental studies with the SML model of this study run using the experiment parameters. Ranges of I_2 emissions represent the range of both measured and calculated flux from the range of experimental inputs used. Model results were obtained with $R = 1$ as no organics are present in these experimental results.

Study	O_3 [ppbv]	Iodide [nM]	Stirred	Temperature [°C]	I_2 emission [molec. cm^{-2} s−1]	Model prediction [molec. cm^{-2} s−1]
Carpenter et al. (2013) [a]	70	10 000–30 000	Yes	18	0.6–1.8 × 10^{11}	0.2–0.3 × 10^{11}
MacDonald et al. (2014) [b]	222	1000	No	3–25	13 ± 4 × 10^9	0.3–1.1 × 10^9
Tinel et al. (2020) [c]	20–110	1200	Yes	17	3–10 × 10^8	7.3–40 × 10^8
Tinel et al. (2020) [c]	34.7	400–10 000	Yes	17	2–100 × 10^8	2.9–78 × 10^8
Schneider et al. (2023) [d]	95–110	390	No	22–25	7.7 × 10^9	0.2–0.6 × 10^9

[a] The pH 8 seawater spiked with iodide. [b] The pH 8 buffered solution with 0.5 M chloride and 1×10^{-6} M iodide. [c] Artificial seawater containing iodide, bromide, and chloride that has been buffered to pH 8. [d] Iodide only with a buffered pH 8 value.

9 Parameterized equation for HOI and I_2 emission flux

Here we present two mathematical functions to predict HOI (Eq. 18) and I_2 (Eq. 19) emission fluxes based on $[O_3]$, bulk $[I^-]$, wind speed, and SST. A non-linear least-squares fit was used on 5000 unique combinations of model inputs covering environmentally comparable ranges of each variable (5–60 ppb of O_3, 0.1–11.1 m s^{-1} wind speed, 20–240 nM bulk $[I^-]$, and 274–300 K SST). All other parameters are kept con-
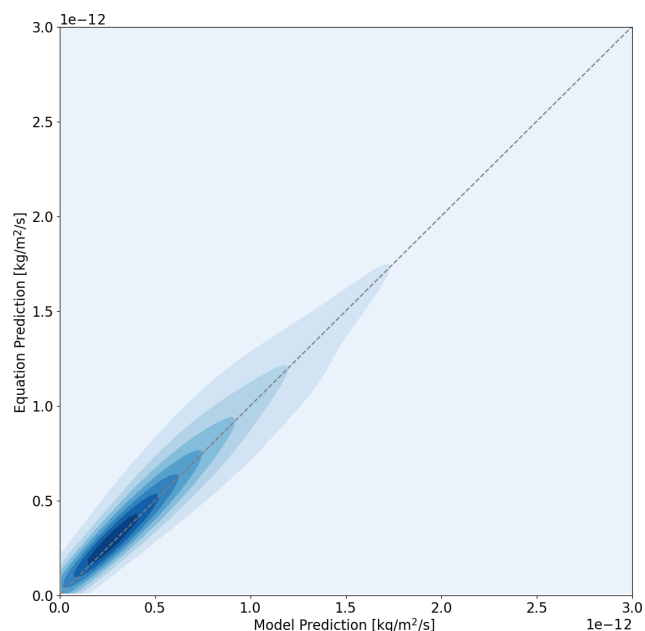
Figure 11. Correlation between modelled total inorganic iodine emission and the sum of $HOI + I_2$ predicted using Eqs. (18) and (19).

stant in the sensitivity analysis. The model sensitivity studies are run using the $O_3 + I^-$ rate from Brown et al. (2024) and the updated equilibrium of Reaction R15b from Schneider et al. (2023). These equations have a high correlation with the results from the SML box model, i.e. $R^2 = 0.92$ for HOI and $R^2 = 0.92$ for I_2, and no strong bias in terms of overestimating or underestimating the model results (Fig. 11).

$$HOI = 6.9 \times 10^{-11} \left(\frac{u + 6.2}{12} \right) e^{-0.034T - \left(\frac{u + 6.2}{12} \right)^2}$$
$$[O_3]_g^{0.92} [I^-]^{0.64} \tag{18}$$

$$I_2 = 4.2 \times 10^{-19} \left(\frac{u + 3.1}{7.2} \right) e^{0.011T - \left(\frac{u + 3.1}{7.2} \right)^2}$$
$$[O_3]_g^{0.73} [I^-]^{1.5} \tag{19}$$

Here HOI and I_2 emission are given in $kg\,m^{-2}\,s^{-1}$, T is the sea surface temperature (K), u is the 10 m wind speed ($m\,s^{-1}$), $[I^-]$ is the bulk water iodide concentration (nM), and $[O_3]_g$ is the atmospheric ozone mixing ratio (ppb).

The most notable difference between the parameterized equations presented here and those from Carpenter et al. (2013) is the inclusion of T as a parameter. Carpenter et al. (2013) found a linear relationship between both HOI and I_2 emissions and atmospheric O_3. This relationship with O_3 is reduced for HOI, which can be attributed to the impact of I^- depletion in the SML being increased at higher O_3 concentrations, reducing the rate at which the $O_3 + I^-$ reaction can occur. The effect of O_3 concentration on I^- depletion

is further enhanced for I_2 production (and hence a further reduction in the I_2 dependence on O_3 concentration) as the subsequent chemical pathways to convert HOI to I_2 also depend on the availability of I^- in the SML. I^- depletion can also explain the increase in dependence of HOI emission on SML $[I^-]$ (from a power of 0.5 to 0.63) and I_2 (from a power of 1.3 to 1.5) due to a relative increase in the availability of I^- in the SML at higher bulk water concentrations.

10 Implementing the new iodine emission equations in GEOS-Chem Classic

We use the GEOS-Chem classic model (Bey et al., 2001) version 14.1.1 (GCC14.1.1, 2023) for global modelling of inorganic iodine emissions and their impact on tropospheric composition. GEOS-Chem Classic is a chemical transport model with a HO_x–NO_x–VOC–O_3–halogen–aerosol tropospheric chemistry scheme. The current version of the halogen chemistry scheme is described by Wang et al. (2021), with organic iodine emissions based on Ordóñez et al. (2012) and inorganic iodine emissions based on Carpenter et al. (2013) (as implemented by Sherwen et al., 2016). The current inorganic iodine emissions in GEOS-Chem use surface oceanic iodide concentrations based on MacDonald et al. (2014), which under-predicts concentrations compared to observations (Sherwen et al., 2019) and differs from the iodide field used in calculating O_3 dry deposition, which uses Sherwen et al. (2019) (Pound et al., 2020). Here, we implement the equations for inorganic iodine emission presented in Sect. 8 and compare the impact of changing the iodide used from MacDonald et al. (2014) to the up-to-date and machine-learning-derived iodide climatology from Sherwen et al. (2019) for both inorganic iodine emissions, providing symmetry with the current use of this iodide climatology in O_3 dry deposition.

A global spatial resolution of $4° × 5°$ on the standard vertical grid (72 vertical levels) is used, running with chemistry in both the troposphere and stratosphere. Meteorological data are from MERRA-2 (Gelaro et al., 2017). Three model runs that were identical in configuration were conducted, with the only difference being their inorganic iodine emissions. The first uses the default inorganic iodine emissions based on the equations from Carpenter et al. (2013) driven by MacDonald et al. (2014) oceanic I^-. The second uses the new iodine emission equations presented in this work (Eqs. 18 and 19) driven by MacDonald et al. (2014) oceanic I^-. The third uses the new iodine emission equations driven by Sherwen et al. (2019) oceanic I^-. All other emission and time step configurations were left at their recommended settings. Model simulations were conducted from 1 July 2019 to 1 July 2021, with the first year of the simulation considered a "spin-up" to allow the model to reach equilibrium. Although the 2020–2021 period is within a La Niña event, a change in temperature of 1 K changes total inorganic iodine emissions by $\sim 3\%$

(Fig. 10). As such, temperature variations due to El Niño–Southern Oscillation (ENSO) are likely to result in changes in the inorganic iodine concentrations of less than 10 % locally and likely even less globally.

The new iodine emission equations decrease the total global inorganic iodine emissions from 2.84 to 2.78 Tg yr^{-1}, a decrease of 2 %. Additionally, there is a slight increase in the ratio of I$_2$ emissions compared to HOI, with I$_2$ now accounting for 5.9 % (previously 5.7 %); however, this difference would not change the impact of iodine on the troposphere as both HOI and I$_2$ rapidly photolyse. Whilst this is a relatively small global total change, there is a significant redistribution of total iodine emissions, with emissions from equatorial waters decreasing and high-latitude emissions increasing, as shown in Fig. 12a. The changes in global emission distribution are largely driven by the change from the Magi et al. (1997) to the Brown et al. (2024) rate constant, with large increases in high-latitude waters also being the result of the base model predicting near-zero emissions in cold waters with low [I$^-$]. Combining the new iodine emission equations with the Sherwen et al. (2019) (Fig. 12b) iodide climatology results in an additional factor of ~ 4 increase in total inorganic iodine emission from high-latitude waters, decreasing to ~ 1.5 outside of these regions. This iodide climatology increases the total global inorganic iodine emissions to 4.5 Tg yr^{-1} (+49 %). Due to the substantially improved comparison with observations, the iodide climatology from Sherwen et al. (2019) will be used in the following analysis.

The change in the distribution of inorganic iodine emissions substantially increases high-latitude IO (and IO$_x$) concentrations, with percentage changes of > 1000 %, as the base case model predicts very low or no IO concentration in these regions (Fig. 13). Equatorial IO has small regional increases and some decreases, mirroring the negligible increases and localized decreases in inorganic iodine emissions from warm waters. However, despite large regional changes, the change in area-weighted mean vertical iodine speciation is minimal, with large percentage changes reflecting small absolute increases. Figure 14 compares published observations of average daytime surface IO mixing ratios to the model predictions from the corresponding day of the year during the simulated period. This comparison only considers open-ocean observations, whereas coastal observations of IO have large influences from macro-algae emissions (Saiz-Lopez and Plane, 2004) that are not included in this model. The change in iodine emissions has little effect on the average model root-mean-square error in atmospheric IO, increasing it from 0.48 to 0.62 ppt (0.43 to 0.58 ppt excluding polar observations), with a change in the relative mean bias from -0.43 to 0.43 ppt (-0.07 to 0.55 ppt excluding polar observations), suggesting that there are still uncertainties in other aspects of our understanding of the iodine system, such as the formation of HIO$_3$ (He et al., 2021; Huang et al., 2022) and the photolysis scheme currently used for higher-iodine oxides (Sherwen et al., 2016). Work to fur-
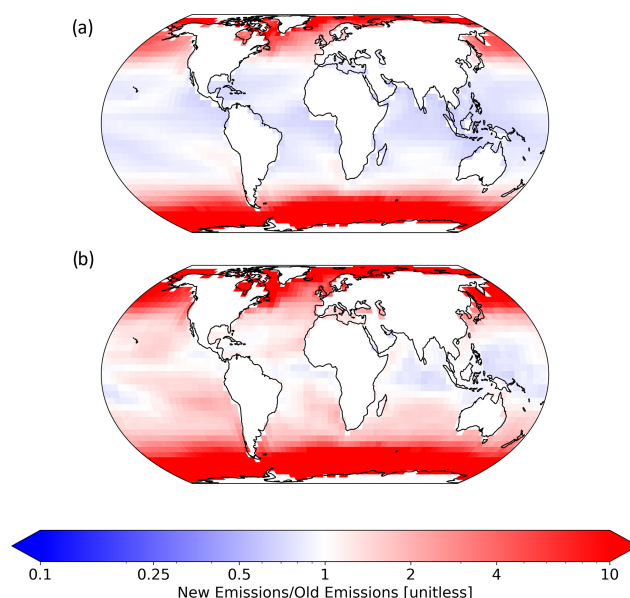

Figure 12. (a) Fractional change in the annual mean total inorganic iodine emissions from Carpenter et al. (2013) equations and MacDonald et al. (2014) (base) I$^-$ to the new HOI and I$_2$ emission equations (Eqs. 18 and 19) and MacDonald et al. (2014). Panel **(b)** shows the change from base to the new HOI and I$_2$ emission equations and Sherwen et al. (2019) I$^-$. The new version of inorganic iodine emission equations combined with Sherwen et al. (2019) sea surface iodide predicts higher emissions at higher latitudes and a decrease in emissions from warmer tropical waters.

ther understand the atmospheric chemistry of iodine is still required if we are to have confidence in the predictions of our models. Wang et al. (2021) found less disagreement between their model and observation comparisons; however, that study included sea salt debromination, which has a large impact on tropospheric O$_3$ and is by default deactivated in version 14.1.1 of GEOS-Chem. The increase in high-latitude oceanic emissions of HOI and I$_2$ reduces the model error at the two Antarctic locations (Bharati and Maitri bases) and the MOSAiC Arctic observations included in Fig. 14. However, the model still significantly underestimates IO levels in the Antarctic region. Atmospheric iodine observations made in the Antarctic region have been shown to have a source from sea ice (Saiz-Lopez et al., 2007; Atkinson et al., 2012) and a direct source of atmospheric IO from the snowpack (Frieß et al., 2010); these processes are not currently represented in the model.

Despite the large increase in total inorganic iodine emissions, there is only a 1.5 % decrease in the tropospheric O$_3$ burden (from 330 to 325 Tg). As with IO, there are larger regional changes in both surface and zonal O$_3$, as shown in Fig. 15. Tropospheric O$_3$ at higher latitudes is decreased with the largest absolute and percentage changes above the Southern Ocean, while O$_3$ above the equatorial Indian Ocean and western central Pacific Ocean increases.
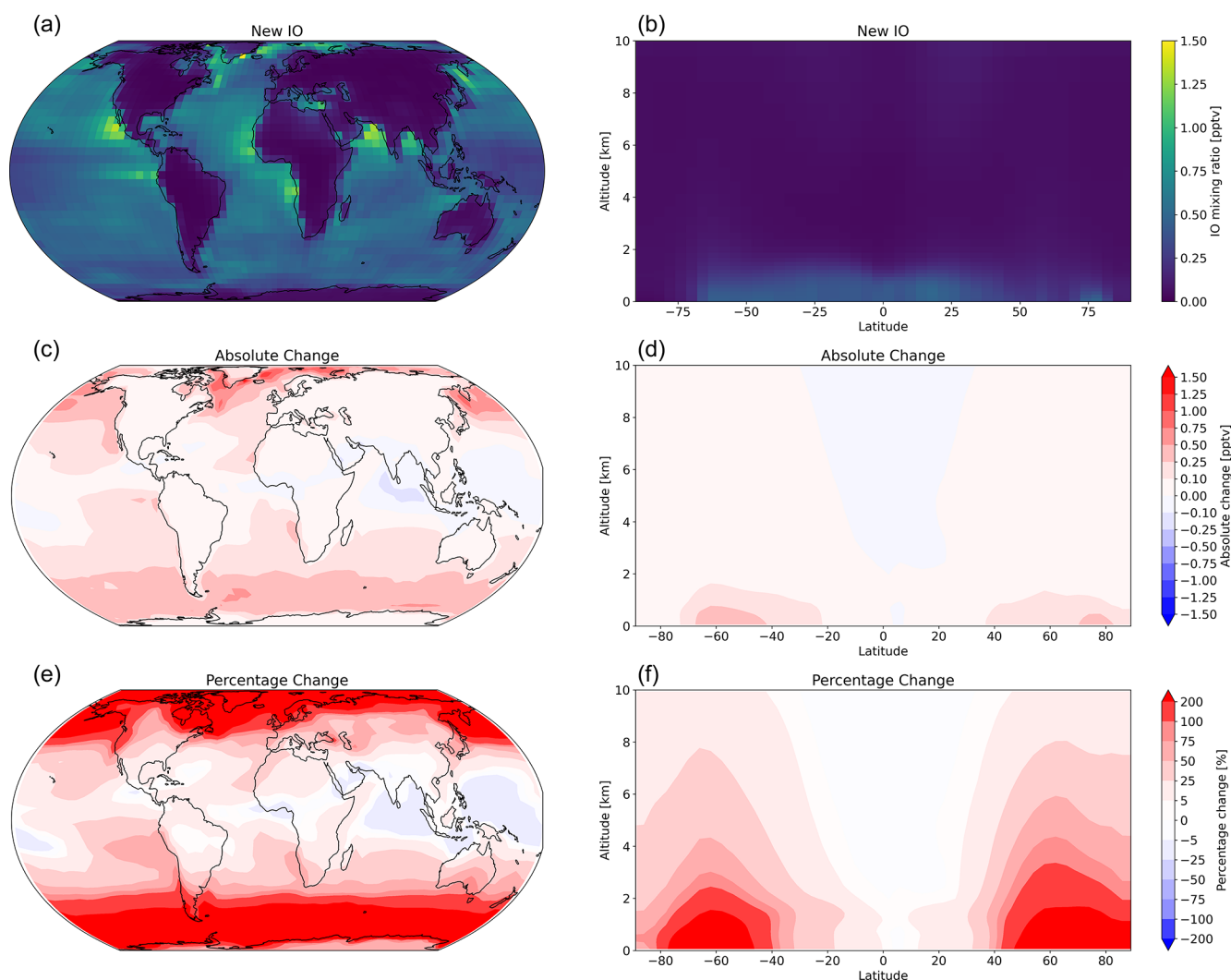
Figure 13. Annual mean mixing ratio of IO **(a, b)** using new inorganic iodine emissions and absolute change **(c, d)** and percentage change **(e, f)** in the annual mean atmospheric IO from implementing the new inorganic iodine emissions relative to the "base" model case, which used oceanic iodine emissions from Carpenter et al. (2013) and iodide from MacDonald et al. (2014).

Figure 16 shows the impact of the change in iodine emissions on surface ozone predictions. For this, we compare the model to a selection of surface ozone measurements from several World Meteorological Organization (WMO) Global Atmosphere Watch sites around the world (GAW; http://www.wmo.int/pages/prog/arep/gaw/gaw_home_en.html, last access: October 2023, accessed through EBAS http://ebas.nilu.no/, last access: October 2023; the database infrastructure is operated by the Norwegian Institute for Air Research).

At the northern high latitudes, we compare to O_3 observations made in Greenland (Fig. 16a). The model disagreement at this site, measured using the root-mean-square error (RMSE), increases from 3.7 to 3.8 ppb (2.7 %); however, the model remains unable to replicate springtime O_3 depletion events that occur in the high latitudes.

Mace Head, Ireland (Fig. 16b), observes air masses that inflow into Europe from the North Atlantic. The model predictions remain within the observed range; however, monthly mean RMSE increases by 38 % (from 3.9 to 5.4 ppbv). Model error in surface O_3 at remote tropical locations, such as the Cape Verde Atmospheric Observatory (CVAO) in Cabo Verde (Fig. 16c), is generally low (2.2 ppbv). The decrease in inorganic iodine emissions from the ocean surrounding these islands increases this error (3.5 ppbv, +59 %); however, like Mace Head, the model remains within the observed range, with the increase in error being most notable during spring.

Comparisons between GEOS-Chem and O_3 observations in the Antarctic and Southern Ocean have consistently shown a low bias in the model (Young et al., 2013; Sherwen et al., 2016; Schmidt et al., 2016; Pound et al., 2020). As with northern high latitudes, the model is also unable to replicate
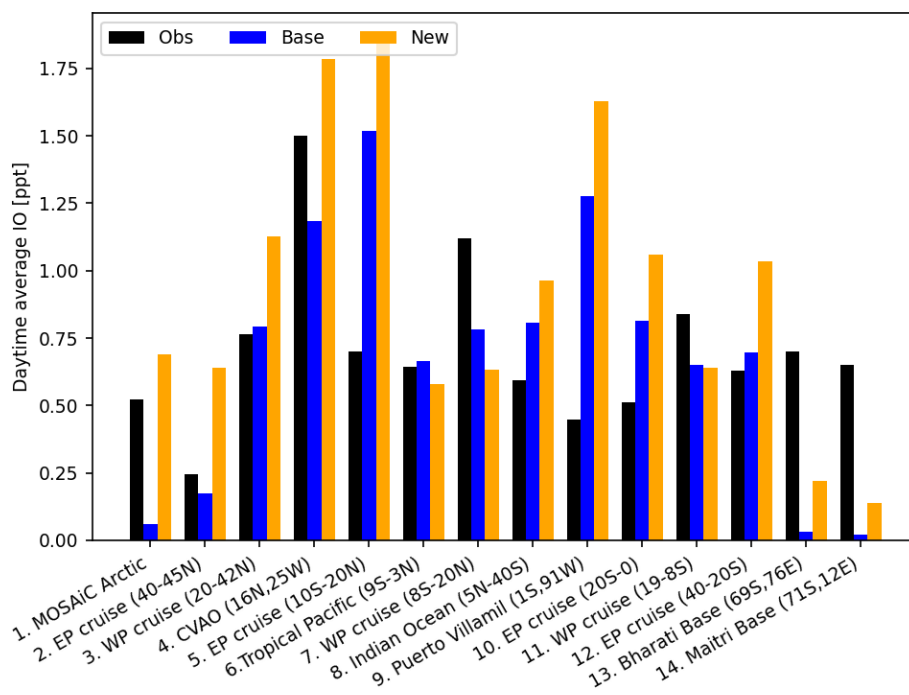
Figure 14. Daytime surface average IO mixing ratio from coastal sites and ocean cruises with observations (black) from reporting periods in different years. Model values are monthly mean daytime surface values taken from the same reporting month and location but from the years 2020/2021, where the base data set (blue) uses HOI and I_2 emissions from Carpenter et al. (2013) driven by MacDonald et al. (2014) iodide and the new data set (orange) uses the HOI and I_2 emissions presented in this work driven by Sherwen et al. (2019) iodide. References are as follows: (1) Mahajan (2022), (2, 5, 10, 12) Mahajan et al. (2012), (3, 7, 11) Großmann et al. (2013), (4) Mahajan et al. (2010), (6) Takashima et al. (2022), (8) Mahajan et al. (2019a, b), (9) Gómez Martín et al. (2013), (13, 14) Mahajan et al. (2021).

halogen-driven O_3 depletion events that occur during Antarctic spring. The decrease in surface O_3 concentrations over the Southern Ocean and Antarctic caused by the increase in Southern Ocean inorganic iodine emissions exacerbates the underestimate of O_3 observations made at Neumayer and Cape Grim (Fig. 16d and f), increasing RMSE by 56 % (from 4.5 to 7.0 ppbv) and 83 % (from 1.8 to 3.3 ppbv), respectively. The third Southern Hemisphere location of Ushuaia (Fig. 16e) has a small increase in model error (5 %, from 2.4 to 2.5 ppbv). The large increase in the error for the Southern Ocean surface O_3, which still shows large underestimates in surface IO, further indicates missing processes in our understanding of Antarctic O_3.

While there are times of better or worse agreement between the model and observations at all locations presented in Fig. 16, model failure is likely not strongly influenced by year-to-year variability in the iodine emissions. Overall, uncertainties in the chemistry, transport, and deposition of iodine species, together with errors and uncertainties in the emission of other species (NO_x, VOCs, halogens, particulate), will combine to provide the overall error profile. There is negligible change in area-weighted mean tropospheric OH concentration and tropospheric CH_4 lifetime (both < 0.2 %).

11 Conclusions

Here we present a new SML box model that incorporates recent advancements in inorganic iodine chemistry and O_3 deposition velocity calculation and improvements to the representation of surface ocean mixing. One key difference between this and previous work is the simulation of depletion of I^- in the SML, which is dependent on the turbulence and the O_3 concentration and has been previously observed in experiments using artificial seawater. This results in a dampening of iodine emissions in low-wind-speed conditions.

From this new box model, we derive parameterized equations for HOI and I_2 emissions that can then be implemented in global models. Using these updated equations in GEOS-Chem combined with the most accurate iodide climatology currently available results in a large increase in total global inorganic iodine emissions (+49 %) and a small decrease in modelled tropospheric O_3 burden (−1.5 %). However, it does result in some local reductions in inorganic iodine emissions in equatorial waters and substantially increased emissions from high-latitude waters.

There are still several uncertainties that remain in oceanic iodine chemistry, atmospheric iodine chemistry, and the emissions of iodine from the SML that have not been addressed by this work. In particular, the model does not ac-
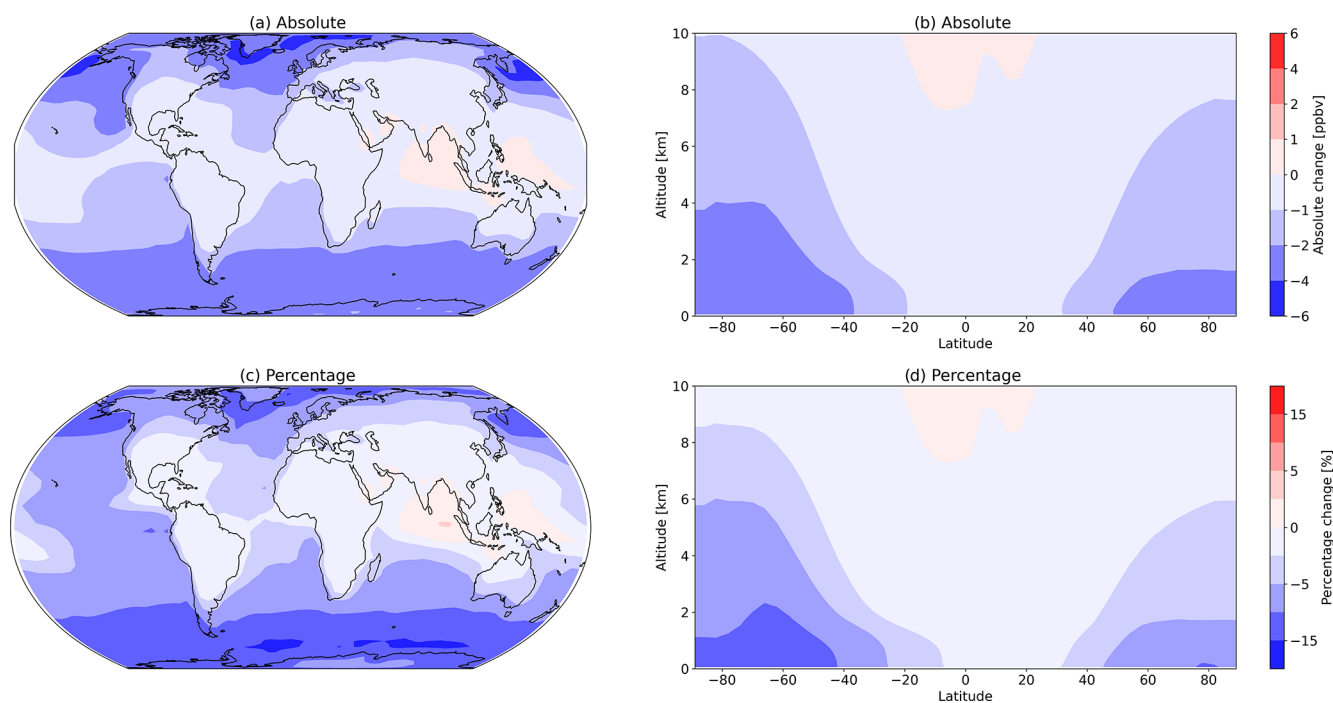
Figure 15. Absolute and percentage change in surface O_3 **(a, c)** and absolute and percentage change in zonal O_3 **(b, d)** due to changing the Carpenter et al. (2013) inorganic iodine emissions from the ocean to the equations presented in this work. The largest changes occur in the surface levels of the model, with the largest relative decrease in surface O_3 occurring over the Southern Ocean and the largest relative increase occurring over the Indian Ocean.
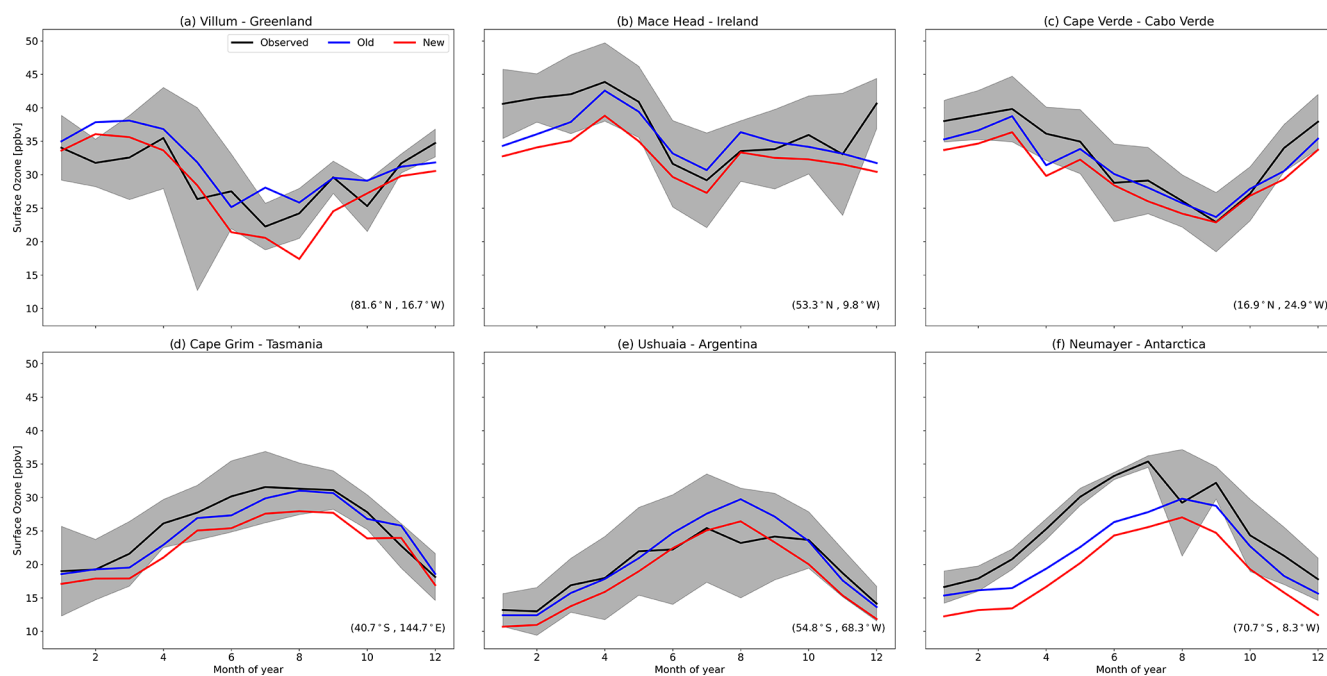

Figure 16. Predictions and observations of monthly average surface ozone mixing ratio from the model using the old iodine emissions (old) and the model using Eqs. (18) and (19) (new) for six GAW stations (with the latitude and longitude for each station at the bottom right), with the shaded region representing the 25th to 75th percentiles. Observational data are from 2014.

count for organic–iodine or organic–ozone interactions in the SML or surfactants suppressing ocean–atmosphere exchange. These processes are not sufficiently well understood to include in models but should be a focus of future work.

Code availability. GEOS-Chem source code is openly available on GitHub (https://github.com/geoschem/geos-chem, last access: 6 September 2024). This work used model version 14.1.1 (https://doi.org/10.5281/zenodo.7696651, GCC14.1.1, 2023).

The box model developed here has been made publicly available on GitHub (https://github.com/r-pound/COAGEM, last access: 6 September 2024) as version 1.1.0 (Pound et al., 2024).

Data availability. The complete results for sensitivity runs used to produce the parameterized HOI and I_2 have been archived and are openly available (Pound et al., 2023a).

Author contributions. RJP performed model development, conducted the simulations, and analysed the output. LVB contributed to model development and analysis. MJE, LJC, and RJP developed the project. All authors contributed to the writing of the manuscript.

Competing interests. The contact author has declared that none of the authors has any competing interests.

Disclaimer. Publisher's note: Copernicus Publications remains neutral with regard to jurisdictional claims made in the text, published maps, institutional affiliations, or any other geographical representation in this paper. While Copernicus Publications makes every effort to include appropriate place names, the final responsibility lies with the authors.

Review statement. This paper was edited by Thorsten Bartels-Rausch and reviewed by two anonymous referees.

References

Alicke, B., Hebestreit, K., Stutz, J., and Platt, U.: Iodine oxide in the marine boundary layer, Nature, 397, 572–573, https://doi.org/10.1038/17508, 1999.

Allan, B. J., McFiggans, G., Plane, J. M. C., and Coe, H.: Observations of iodine monoxide in the remote marine boundary layer, J. Geophys. Res.-Atmos., 105, 14363–14369, https://doi.org/10.1029/1999JD901188, 2000.

Amachi, S.: Microbial Contribution to Global Iodine Cycling: Volatilization, Accumulation, Reduction, Oxidation, and Sorption of Iodine, Microb. Environ., 23, 269–276, https://doi.org/10.1264/jsme2.ME08548, 2008.

Atkinson, H. M., Huang, R.-J., Chance, R., Roscoe, H. K., Hughes, C., Davison, B., Schönhardt, A., Mahajan, A. S., Saiz-Lopez, A., Hoffmann, T., and Liss, P. S.: Iodine emissions from the sea ice of the Weddell Sea, Atmos. Chem. Phys., 12, 11229–11244, https://doi.org/10.5194/acp-12-11229-2012, 2012.

Badia, A., Iglesias-Suarez, F., Fernandez, R. P., Cuevas, C. A., Kinnison, D. E., Lamarque, J.-F., Griffiths, P. T., Tarasick, D. W., Liu, J., and Saiz-Lopez, A.: The Role of Natural Halogens in Global Tropospheric Ozone Chemistry and Budget Under Different 21st Century Climate Scenarios, J. Geophys. Res.-Atmos., 126, e2021JD034859, https://doi.org/10.1029/2021JD034859, 2021.

Barrera, J., Kinnison, D., Fernandez, R., Lamarque, J., Cuevas, C., Tilmes, S., and Saiz-Lopez, A.: Comparing the Effect of Anthropogenically Amplified Halogen Natural Emissions on Tropospheric Ozone Chemistry Between Pre-Industrial and Present-Day, J. Geophys. Res.-Atmos., 128, e2022JD038283, https://doi.org/10.1029/2022JD038283, 2023.

Beckwith, R. C., Wang, T. X., and Margerum, D. W.: Equilibrium and kinetics of bromine hydrolysis, Inorg. Chem., 35, 995–1000, 1996.

Bey, I., Jacob, D. J., Yantosca, R. M., Logan, J. A., Field, B. D., Fiore, A. M., Li, Q., Liu, H. Y., Mickley, L. J., and Schultz, M. G.: Global modeling of tropospheric chemistry with assimilated meteorology: Model description and evaluation, J. Geophys. Res.-Atmos., 106, 23073–23095, https://doi.org/10.1029/2001JD000807, 2001.

Bichsel, Y. and von Gunten, U.: Hypoiodous acid: kinetics of the buffer-catalyzed disproportion, Water Res., 34, 3197–3203, https://doi.org/10.1016/S0043-1354(00)00077-4, 2000.

Bloss, W. J., Lee, J. D., Johnson, G. P., Sommariva, R., Heard, D. E., Saiz-Lopez, A., Plane, J. M. C., McFiggans, G., Coe, H., Flynn, M., Williams, P., Rickard, A. R., and Fleming, Z. L.: Impact of halogen monoxide chemistry upon boundary layer OH and HO_2 concentrations at a coastal site, Geophys. Res. Lett., 32, 6, https://doi.org/10.1029/2004GL022084, 2005.

Brown, L. V., Pound, R. J., Ives, L. S., Jones, M. R., Andrews, S. J., and Carpenter, L. J.: Negligible temperature dependence of the ozone–iodide reaction and implications for oceanic emissions of iodine, Atmos. Chem. Phys., 24, 3905–3923, https://doi.org/10.5194/acp-24-3905-2024, 2024.

Carpenter, L., Chance, R. J., Sherwen, T., Adams, T. J., Ball, S. M., Evans, M. J., Hepach, H., Hollis, L. D. J., Hughes, C., Jickells, T. D., Mahajan, A., Stevens, D. P., Tinel, L., and Wadley, M. R.: Marine iodine emissions in a changing world, P. Roy. Soc. A, 477, 20200824, https://doi.org/10.1098/rspa.2020.0824, 2021.

Carpenter, L. J. and Nightingale, P. D.: Chemistry and release of gases from the surface ocean,, Chem. Rev., 115, 4015–4034, https://doi.org/10.1021/cr5007123, 2015.

Carpenter, L. J., MacDonald, S. M., Shaw, M. D., Kumar, R., Saunders, R. W., Parthipan, R., Wilson, J., and Plane, J. M. C.: Atmospheric iodine levels influenced by sea surface emissions of inorganic iodine, Nat. Geosc., 6, 108–111, https://doi.org/10.1038/ngeo1687, 2013.

Cen-Lin, H. and Tzung-May, F.: Air-Sea Exchange of Volatile Organic Compounds: A New Model with Microlayer Effects, Atmos. Ocean. Sci. Lett., 6, 97–102, https://doi.org/10.1080/16742834.2013.11447063, 2013.

Chance, R., Malin, G., Jickells, T., and Baker, A. R.: Reduction of iodate to iodide by cold water diatom cultures, Mar. Chem., 105, 169–180, https://doi.org/10.1016/j.marchem.2006.06.008, 2007.

Chance, R., Baker, A. R., Carpenter, L., and Jickells, T. D.: The distribution of iodide at the sea surface, Environ. Sci.: Proc. Imp., 16, 1841–1859, https://doi.org/10.1039/C4EM00139G, 2014.

Chance, R., Tinel, L., Sarkar, A., Sinha, A. K., Mahajan, A. S., Chacko, R., Sabu, P., Roy, R., Jickells, T. D., Stevens, D. P., Wadley, M., and Carpenter, L. J.: Surface Inorganic Iodine Speciation in the Indian and Southern Oceans From 12° N to 70° S, Front. Mar. Sci., 7, https://doi.org/10.3389/fmars.2020.00621, 2020.

Chang, W., Heikes, B., and Lee, M.: Ozone deposition to the sea surface:chemical enhancement and wind speed dependence, Atmos. Environ., 38, 1053–1059, https://doi.org/10.1016/j.atmosenv.2003.10.050, 2004.

Citri, O. and Epstein, I. R.: Mechanistic Study of a Coupled Chemical Oscillator: The Bromate-Chlorite Iodide Reaction, J. Phys. Chem., 92, 1865–1871 https://doi.org/10.1021/j100318a034, 1988.

Cuevas, C. A., Maffezzoli, N., Corella, J. P., Spolaor, A., Vallelonga, P., Kjær, H. A., Simonsen, M., Winstrup, M., Vinther, B., Horvat, C., Fernandez, R. P., Kinnison, D., Lamarque, J.-F., Barbante, C., and Saiz-Lopez, A.: Rapid increase in atmospheric iodine levels in the North Atlantic since the mid-20th century, Nat. Commun., 9, 1452, https://doi.org/10.1038/s41467-018-03756-1, 2018.

Cuevas, C. A., Fernandez, R. P., Kinnison, D. E., Li, Q., Lamarque, J.-F., Trabelsi, T., Francisco, J. S., Solomon, S., and Saiz-Lopez, A.: The influence of iodine on the Antarctic stratospheric ozone hole, P. Natl. Acad. Sci. USA, 119, e2110864119, https://doi.org/10.1073/pnas.2110864119, 2022.

Cunliffe, M., Engel, A., Frka, S., Gašparović, B., Guitart, C., Murrell, J. C., Salter, M., Stolle, C., Upstill-Goddard, R., and Wurl, O.: Sea surface microlayers: A unified physicochemical and biological perspective of the air–ocean interface, Prog. Oceanogr., 109, 104–116, https://doi.org/10.1016/j.pocean.2012.08.004, 2013.

De Barros Faria, R., Lengyel, I., Epstein, I. R., and Kustin, K.: Systematic design of chemical oscillators. 86. Combined mechanism explaining nonlinear dynamics in bromine(III) and bromine(V) oxidations of iodide ion, J. Phys. Chem., 97, 1164–1171, https://doi.org/10.1021/j100108a011, 1993.

The Pandas development team: pandas-dev/pandas: Pandas, Zenodo [code], https://doi.org/10.5281/zenodo.3509134, 2020.

Fairall, C. W., Helmig, D., Ganzeveld, L., and Hare, J.: Waterside turbulence enhancement of ozone deposition to the ocean, Atmos. Chem. Phys., 7, 443–451, https://doi.org/10.5194/acp-7-443-2007, 2007.

Frew, N. M., Goldman, J. C., Dennett, M. R., and Johnson, A. S.: Impact of phytoplankton-generated surfactants on air-sea gas exchange, J. Geophys. Res.-Oceans, 95, 3337–3352, https://doi.org/10.1029/JC095iC03p03337, 1990.

Frieß, U., Deutschmann, T., Gilfedder, B. S., Weller, R., and Platt, U.: Iodine monoxide in the Antarctic snowpack, Atmos. Chem. Phys., 10, 2439–2456, https://doi.org/10.5194/acp-10-2439-2010, 2010.

Ganzeveld, L., Helmig, D., Fairall, C., Hare, J., and Pozzer, A.: Atmosphere-ocean ozone exchange: A global modeling study of biogeochemical, atmospheric, and waterside turbulence dependencies, Global Biogeochem. Cy., 23, https://doi.org/10.1029/2008GB003301, 2009.

Garland, J. A., Elzerman, A. W., and Penkett, S. A.: The mechanism for dry deposition of ozone to seawater surfaces, J. Geophys. Res.-Oceans, 85, 7488–7492, https://doi.org/10.1029/JC085iC12p07488, 1980.

GCC14.1.1: The International GEOS-Chem User Community, geoschem/GCCClassic: GEOS-Chem 14.1.1, Zenodo [code], https://doi.org/10.5281/zenodo.7696651, 2023.

Gelaro, R., McCarty, W., Suárez, M. J., Todling, R., Molod, A., Takacs, L., Randles, C. A., Darmenov, A., Bosilovich, M. G., Reichle, R., Wargan, K., Coy, L., Cullather, R., Draper, C., Akella, S., Buchard, V., Conaty, A., da Silva, A. M., Gu, W., Kim, G.-K., Koster, R., Lucchesi, R., Merkova, D., Nielsen, J. E., Partyka, G., Pawson, S., Putman, W., Rienecker, M., Schubert, S. D., Sienkiewicz, M., and Zhao, B.: The Modern-Era Retrospective Analysis for Research and Applications, Version 2 (MERRA-2), J. Climate, 30, 5419–5454, https://doi.org/10.1175/JCLI-D-16-0758.1, 2017.

Goldman, J., Dennett, M., and Frew, N.: Surfactant effects on air-sea gas exchange under turbulent conditions, Deep-Sea Res. P. A, 35, 1953–1970, https://doi.org/10.1016/0198-0149(88)90119-7, 1988.

Gómez Martín, J. C., Mahajan, A. S., Hay, T. D., Prados-Román, C., Ordóñez, C., MacDonald, S. M., Plane, J. M., Sorribas, M., Gil, M., Paredes Mora, J. F., Agama Reyes, M. V., Oram, D. E., Leedham, E., and Saiz-Lopez, A.: Iodine chemistry in the eastern Pacific marine boundary layer, J. Geophys. Res.-Atmos., 118, 887–904, https://doi.org/10.1002/jgrd.50132, 2013.

Goodwin, D. G., Moffat, H. K., Schoegl, I., Speth, R. L., and Weber, B. W.: Cantera: An Object-oriented Software Toolkit for Chemical Kinetics, Thermodynamics, and Transport Processes, version 2.6.0, Zenodo [code], https://doi.org/10.5281/zenodo.6387882, 2022.

Großmann, K., Frieß, U., Peters, E., Wittrock, F., Lampel, J., Yilmaz, S., Tschritter, J., Sommariva, R., von Glasow, R., Quack, B., Krüger, K., Pfeilsticker, K., and Platt, U.: Iodine monoxide in the

Western Pacific marine boundary layer, Atmos. Chem. Phys., 13, 3363–3378, https://doi.org/10.5194/acp-13-3363-2013, 2013.

Haag, W. R. and Hoigné, J.: Ozonation of bromide-containing waters: Kinetics of formation of hypobromous acid and bromate, Environ. Sci. Technol., 17, 261–267, 1983.

Hao, H., Leven, I., and Head-Gordon, T.: Can electric fields drive chemistry for an aqueous microdroplet?, Nat. Commun., 13, https://doi.org/10.1038/s41467-021-27941-x, 2022.

Hardacre, C., Wild, O., and Emberson, L.: An evaluation of ozone dry deposition in global scale chemistry climate models, Atmos. Chem. Phys., 15, 6419–6436, https://doi.org/10.5194/acp-15-6419-2015, 2015.

Harris, C. R., Millman, K. J., van der Walt, S. J., Gommers, R., Virtanen, P., Cournapeau, D., Wieser, E., Taylor, J., Berg, S., Smith, N. J., Kern, R., Picus, M., Hoyer, S., van Kerkwijk, M. H., Brett, M., Haldane, A., del Río, J. F., Wiebe, M., Peterson, P., Gérard-Marchant, P., Sheppard, K., Reddy, T., Weckesser, W., Abbasi, H., Gohlke, C., and Oliphant, T. E.: Array programming with NumPy, Nature, 585, 357–362, https://doi.org/10.1038/s41586-020-2649-2, 2020.

He, X.-C., Tham, Y. J., Dada, L., Wang, M., Finkenzeller, H., Stolzenburg, D., Iyer, S., Simon, M., Kürten, A., Shen, J., Rörup, B., Rissanen, M., Schobesberger, S., Baalbaki, R., Wang, D. S., Koenig, T. K., Jokinen, T., Sarnela, N., Beck, L. J., Almeida, J., Amanatidis, S., Amorim, A., Ataei, F., Baccarini, A., Bertozzi, B., Bianchi, F., Brilke, S., Caudillo, L., Chen, D., Chiu, R., Chu, B., Dias, A., Ding, A., Dommen, J., Duplissy, J., Haddad, I. E., Carracedo, L. G., Granzin, M., Hansel, A., Heinritzi, M., Hofbauer, V., Junninen, H., Kangasluoma, J., Kemppainen, D., Kim, C., Kong, W., Krechmer, J. E., Kvashin, A., Laitinen, T., Lamkaddam, H., Lee, C. P., Lehtipalo, K., Leiminger, M., Li, Z., Makhmutov, V., Manninen, H. E., Marie, G., Marten, R., Mathot, S., Mauldin, R. L., Mentler, B., Möhler, O., Müller, T., Nie, W., Onnela, A., Petäjä, T., Pfeifer, J., Philippov, M., Ranjithkumar, A., Saiz-Lopez, A., Salma, I., Scholz, W., Schuchmann, S., Schulze, B., Steiner, G., Stozhkov, Y., Tauber, C., Tomé, A., Thakur, R. C., Väisänen, O., Vazquez-Pufleau, M., Wagner, A. C., Wang, Y., Weber, S. K., Winkler, P. M., Wu, Y., Xiao, M., Yan, C., Ye, Q., Ylisirniö, A., Zauner-Wieczorek, M., Zha, Q., Zhou, P., Flagan, R. C., Curtius, J., Baltensperger, U., Kulmala, M., Kerminen, V.-M., Kurtén, T., Donahue, N. M., Volkamer, R., Kirkby, J., Worsnop, D. R., and Sipilä, M.: Role of iodine oxoacids in atmospheric aerosol nucleation, Science, 371, 589–595, https://doi.org/10.1126/science.abe0298, 2021.

Hoffmann, T., O'Dowd, C. D., and Seinfeld, J. H.: Iodine oxide homogeneous nucleation: An explanation for coastal new particle production, Geophys. Res. Lett., 28, 1949–1952, https://doi.org/10.1029/2000GL012399, 2001.

Hu, J. H., Shi, Q., Davidovits, P., Worsnop, D. R., Zahniser, M. S., and Kolb, C. E.: Reactive Uptake of Cl2(g) and Br2(g) by Aqueous Surfaces as a Function of Br- and I- Ion Concentration: The Effect of Chemical Reaction at the Interface, J. Phys. Chem., 99, 8768–8776, https://doi.org/10.1021/j100021a050, 1995.

Huang, R.-J., Hoffmann, T., Ovadnevaite, J., Laaksonen, A., Kokkola, H., Xu, W., Xu, W., Ceburnis, D., Zhang, R., Seinfeld, J. H., and O'Dowd, C.: Heterogeneous iodine-organic chemistry fast-tracks marine new particle formation, P. Natl. Acad. Sci. USA, 119, e2201729119, https://doi.org/10.1073/pnas.2201729119, 2022.

Iglesias-Suarez, F., Badia, A., Fernandez, R. P., Cuevas, C. A., Kinnison, D. E., Tilmes, S., Lamarque, J.-F., Long, M. C., Hossaini, R., and Saiz-Lopez, A.: Natural halogens buffer tropospheric ozone in a changing climate, Nat. Clim. Change, 10, 147–154, https://doi.org/10.1038/s41558-019-0675-6, 2020.

Johnson, M. T.: A numerical scheme to calculate temperature and salinity dependent air-water transfer velocities for any gas, Ocean Sci., 6, 913–932, https://doi.org/10.5194/os-6-913-2010, 2010.

Johnson, P. N. and Davis, R. A.: Diffusivity of Ozone in Water, J. Chem. Eng. Data, 41, 1485–1487, https://doi.org/10.1021/je9602125, 1996.

Jones, C. E., Hornsby, K. E., Sommariva, R., Dunk, R. M., von Glasow, R., McFiggans, G., and Carpenter, L. J.: Quantifying the contribution of marine organic gases to atmospheric iodine, Geophys. Res. Lett., 37, https://doi.org/10.1029/2010GL043990, 2010.

Koenig, T. K., Baidar, S., Campuzano-Jost, P., Cuevas, C. A., Dix, B., Fernandez, R. P., Guo, H., Hall, S. R., Kinnison, D., Nault, B. A., Ullmann, K., Jimenez, J. L., Saiz-Lopez, A., and Volkamer, R.: Quantitative detection of iodine in the stratosphere, P. Natl. Acad. Sci. USA, 117, 1860–1866, https://doi.org/10.1073/pnas.1916828117, 2020.

Kumar, K. and Margerum, D. W.: Kinetics and mechanism of general-acid-assisted oxidation of bromide by hypochlorite and hypochlorous acid, Inorg. Chem., 26, 2706–2711, 1987.

Kumar, K., Day, R. A., and Margerum, D. W.: Atom-transfer redox kinetics: general-acid-assisted oxidation of iodide by chloramines and hypochlorite, Inorg. Chem., 25, 4344–4350, https://doi.org/10.1021/ic00244a012, 1986.

Legrand, M., McConnell, J. R., Preunkert, S., Arienzo, M., Chellman, N., Gleason, K., Sherwen, T., Evans, M. J., and Carpenter, L. J.: Alpine ice evidence of a three-fold increase in atmospheric iodine deposition since 1950 in Europe due to increasing oceanic emissions, P. Natl. Acad. Sci. USA, 115, 12136–12141, https://doi.org/10.1073/pnas.1809867115, 2018.

Lengyel, I., Epstein, I. R., and Kustin, K.: Kinetics of iodine hydrolysis, Inorg. Chem., 32, 5880–5882, https://doi.org/10.1021/ic00077a036, 1993.

Lengyel, I., Li, J., Kustin, K., and Epstein, I. R.: Rate Constants for Reactions between Iodine- and Chlorine-Containing Species: A Detailed Mechanism of the Chlorine Dioxide/Chlorite-Iodide Reaction, J. Am. Chem. Soc., 3708–3719, https://doi.org/10.1021/ja953938e, 1996.

Levanov, A. V., Isaikina, O. Y., Gasanova, R. B., Uzhel, A. S., and Lunin, V. V.: Kinetics of chlorate formation during ozonation of aqueous chloride solutions, Chemosphere, 229, 68–76, https://doi.org/10.1016/j.chemosphere.2019.04.105, 2019.

Liu, Q., Schurter, L. M., Muller, C. E., Aloisio, S., Francisco, J. S., and Margerum, D. W.: Kinetics and Mechanisms of Aqueous Ozone Reactions with Bromide, Sulfite, Hydrogen Sulfite, Iodide, and Nitrite Ions, Inorg. Chem., 40, 4436–4442, https://doi.org/10.1021/ic000919j, 2001.

Luhar, A. K., Galbally, I. E., Woodhouse, M. T., and Thatcher, M.: An improved parameterisation of ozone dry deposition to the ocean and its impact in a global climate-chemistry model, Atmos. Chem. Phys., 17, 3749–3767, https://doi.org/10.5194/acp-17-3749-2017, 2017.

Luhar, A. K., Woodhouse, M. T., and Galbally, I. E.: A revised global ozone dry deposition estimate based on a new two-layer

parameterisation for air–sea exchange and the multi-year MACC composition reanalysis, Atmos. Chem. Phys., 18, 4329–4348, https://doi.org/10.5194/acp-18-4329-2018, 2018.

MacDonald, S. ., Gómez Martín, J. C., Chance, R., Warriner, S., Saiz-Lopez, A., Carpenter, L. J., and Plane, J. M. C.: A laboratory characterisation of inorganic iodine emissions from the sea surface: dependence on oceanic variables and parameterisation for global modelling, Atmos. Chem. Phys., 14, 5841–5852, https://doi.org/10.5194/acp-14-5841-2014, 2014.

Magi, L., Schweitzer, F., Pallares, C., Cherif, S., Mirabel, P., and George, C.: Investigation of the Uptake Rate of Ozone and Methyl Hydroperoxide by Water Surfaces, J. Phys. Chem. A, 101, 4943–4949, https://doi.org/10.1021/jp970646m, 1997.

Mahajan, A.: Substantial contribution of iodine to Arctic ozone destruction – data, Mendeley Data [data set], https://doi.org/10.17632/bn7ytz4mfz.1, 2022.

Mahajan, A. S., Plane, J. M. C., Oetjen, H., Mendes, L., Saunders, R. W., Saiz-Lopez, A., Jones, C. E., Carpenter, L. J., and McFiggans, G. B.: Measurement and modelling of tropospheric reactive halogen species over the tropical Atlantic Ocean, Atmos. Chem. Phys., 10, 4611–4624, https://doi.org/10.5194/acp-10-4611-2010, 2010.

Mahajan, A. S., Gómez Martín, J. C., Hay, T. D., Royer, S.-J., Yvon-Lewis, S., Liu, Y., Hu, L., Prados-Roman, C., Ordóñez, C., Plane, J. M. C., and Saiz-Lopez, A.: Latitudinal distribution of reactive iodine in the Eastern Pacific and its link to open ocean sources, Atmos. Chem. Phys., 12, 11609–11617, https://doi.org/10.5194/acp-12-11609-2012, 2012.

Mahajan, A. S., Tinel, L., Hulswar, S., Cuevas, C. A., Wang, S., Ghude, S., Naik, R. K., Mishra, R. K., Sabu, P., Sarkar, A., Anilkumar, N., and Saiz Lopez, A.: Observations of iodine oxide in the Indian Ocean marine boundary layer: A transect from the tropics to the high latitudes, Atmos. Environ. X, 1, 100016, https://doi.org/10.1016/j.aeaoa.2019.100016, 2019a.

Mahajan, A. S., Tinel, L., Sarkar, A., Chance, R., Carpenter, L. J., Hulswar, S., Mali, P., Prakash, S., and Vinayachandran, P. N.: Understanding Iodine Chemistry Over the Northern and Equatorial Indian Ocean, J. Geophys. Res.-Atmos., 124, 8104–8118, https://doi.org/10.1029/2018JD029063, 2019b.

Mahajan, A. S., Biswas, M. S., Beirle, S., Wagner, T., Schönhardt, A., Benavent, N., and Saiz-Lopez, A.: Observations of iodine monoxide over three summers at the Indian Antarctic bases of Bharati and Maitri, Atmos. Chem. Phys., 21, 11829–11842, https://doi.org/10.5194/acp-21-11829-2021, 2021.

Michalowski, B. A., Francisco, J. S., Li, S.-M., Barrie, L. A., Bottenheim, J. W., and Shepson, P. B.: A computer model study of multiphase chemistry in the Arctic boundary layer during polar sunrise, J. Geophys. Res.-Atmos., 105, 15131–15145, https://doi.org/10.1029/2000JD900004, 2000.

Moreno, C. G., Gálvez, O., López-Arza Moreno, V., Espildora-García, E. M., and Baeza-Romero, M. T.: A revisit of the interaction of gaseous ozone with aqueous iodide. Estimating the contributions of the surface and bulk reactions, Phys. Chem. Chem. Phys., 20, 27571–27584, https://doi.org/10.1039/C8CP04394A, 2018.

Morris, J.: The aqueous solubility of ozone – A review, Ozone News, 1, 14–16, 1988.

Nagy, J. C., Kumar, K., and Margerum, D. W.: Non-Metal Redox Kinetics: Oxidation of Iodide by Hypochlorous Acid and by Nitrogen Trichloride Measured by the Pulsed-Accelerated-Flow Method, Inorg. Chem., 27, 2773–2780, https://doi.org/10.1021/ic00289a007, 1988.

Nightingale, P. D., Malin, G., Law, C. S., Watson, A. J., Liss, P. S., Liddicoat, M. I., Boutin, J., and Upstill-Goddard, R. C.: In situ evaluation of air-sea gas exchange parameterizations using novel conservative and volatile tracers, Global Biogeochem. Cy., 14, 373–387, https://doi.org/10.1029/1999GB900091, 2000.

Ordóñez, C., Lamarque, J.-F., Tilmes, S., Kinnison, D. E., Atlas, E. L., Blake, D. R., Sousa Santos, G., Brasseur, G., and Saiz-Lopez, A.: Bromine and iodine chemistry in a global chemistry-climate model: description and evaluation of very short-lived oceanic sources, Atmos. Chem. Phys., 12, 1423–1447, https://doi.org/10.5194/acp-12-1423-2012, 2012.

Paquette, J.: Modelling the chemistry of iodine, Proceedings of the CSNI workshop on iodine chemistry in reactor safety (2nd: 1988: Toronto), 216–234, https://www.oecd-nea.org/jcms/pl_15816/proceedings-of-the-csni-workshop-on-iodine-chemistry-in (last access: October 2023), 1989.

Pound, R., Brown, L., Evans, M., and Carpenter, L.: Coupled Ocean Atmosphere Gas Exchange Model Sensitivity Analysis, University of York, https://doi.org/10.15124/e377ffa4-ede9-490d-8a65-95f3b6d61137, 2023a.

Pound, R. J., Sherwen, T., Helmig, D., Carpenter, L. J., and Evans, M. J.: Influences of oceanic ozone deposition on tropospheric photochemistry, Atmos. Chem. Phys., 20, 4227–4239, https://doi.org/10.5194/acp-20-4227-2020, 2020.

Pound, R. J., Durcan, D. P., Evans, M. J., and Carpenter, L. J.: Comparing the Importance of Iodine and Isoprene on Tropospheric Photochemistry, Geophys. Res. Lett., 50, e2022GL100997, https://doi.org/10.1029/2022GL100997, 2023b.

Pound, R., Brown, L. V., Evans, M. J., and Carpenter, L. J.: Coupled Ocean-Atmosphere Gas Exchange Mode, V1.1.0, Zenodo [code], https://doi.org/10.5281/zenodo.10634463, 2024.

Prados-Roman, C., Cuevas, C. A., Hay, T., Fernandez, R. P., Mahajan, A. S., Royer, S.-J., Galí, M., Simó, R., Dachs, J., Großmann, K., Kinnison, D. E., Lamarque, J.-F., and Saiz-Lopez, A.: Iodine oxide in the global marine boundary layer, Atmos. Chem. Phys., 15, 583–593, https://doi.org/10.5194/acp-15-583-2015, 2015.

Reeser, D. and Donaldson, D.: Influence of water surface properties on the heterogeneous reaction between $O_{3(g)}$ and $I^-_{(aq)}$, Atmos. Environ., 45, 6116–6120, https://doi.org/10.1016/j.atmosenv.2011.08.042, 2011.

Rouvière, A. and Ammann, M.: The effect of fatty acid surfactants on the uptake of ozone to aqueous halogenide particles, Atmos. Chem. Phys., 10, 11489–11500, https://doi.org/10.5194/acp-10-11489-2010, 2010.

Saiz-Lopez, A. and Plane, J. M. C.: Novel iodine chemistry in the marine boundary layer, Geophys. Res. Lett., 31, https://doi.org/10.1029/2003GL019215, 2004.

Saiz-Lopez, A., Mahajan, A. S., Salmon, R. A., Bauguitte, S. J.-B., Jones, A. E., Roscoe, H. K., and Plane, J. M. C.: Boundary Layer Halogens in Coastal Antarctica, Science, 317, 348–351, https://doi.org/10.1126/science.1141408, 2007.

Saiz-Lopez, A., Plane, J. M. C., Baker, A. R., Carpenter, L. J., von Glasow, R., Gómez Martín, J. C., McFiggans, G., and Saunders, R. W.: Atmospheric Chemistry of Iodine, Chem. Rev., 112, 1773–1804, https://doi.org/10.1021/cr200029u, 2012.

Saiz-Lopez, A., Baidar, S., Cuevas, C. A., Koenig, T. K., Fernandez, R. P., Dix, B., Kinnison, D. E., Lamarque, J.-F., Rodriguez-Lloveras, X., Campos, T. L., and Volkamer, R.: Injection of iodine to the stratosphere, Geophys. Res. Lett., 42, 6852–6859, https://doi.org/10.1002/2015GL064796, 2015.

Saiz-Lopez, A., Fernandez, R. P., Li, Q., Cuevas, C. A., Fu, X., Kinnison, D. E., Tilmes, S., Mahajan, A. S., Gómez Martín, J. C., Iglesias-Suarez, F., Hossaini, R., Plane, J. M. C., Myhre, G., and Lamarque, J.-F.: Natural short-lived halogens exert an indirect cooling effect on climate, Nature, 618, 967–973, https://doi.org/10.1038/s41586-023-06119-z, 2023.

Schmidt, J. A., Jacob, D. J., Horowitz, H. M., Hu, L., Sherwen, T., Evans, M. J., Liang, Q., Suleiman, R. M., Oram, D. E., Le Breton, M., Percival, C. J., Wang, S., Dix, B., and Volkamer, R.: Modeling the observed tropospheric BrO background: Importance of multiphase chemistry and implications for ozone, OH, and mercury, J. Geopphys. Res.-Atmos., 121, 11819–11835, https://doi.org/10.1002/2015JD024229, 2016.

Schneider, S. R., Lakey, P. S. J., Shiraiwa, M., and Abbatt, J. P. D.: Reactive Uptake of Ozone to Simulated Seawater: Evidence for Iodide Depletion, J. Phys. Chem. A, 124, 9844–9853, https://doi.org/10.1021/acs.jpca.0c08917, 2020.

Schneider, S. R., Lakey, P. S. J., Shiraiwa, M., and Abbatt, J. P. D.: Iodine emission from the reactive uptake of ozone to simulated seawater, Environ. Sci.: Proc. Imp., 25, 254–263, https://doi.org/10.1039/D2EM00111J, 2023.

Sebők-Nagy, K. and Körtvélyesi, T.: Kinetics and mechanism of the hydrolytic disproportionation of iodine, Int. J. Chem. Kinet., 36, 596–602, https://doi.org/10.1002/kin.20033, 2004.

Shaw, M. D. and Carpenter, L. J.: Modification of Ozone Deposition and I2 Emissions at the Air–Aqueous Interface by Dissolved Organic Carbon of Marine Origin, Environ. Sci. Technol., 47, 10947–10954, https://doi.org/10.1021/es4011459, 2013.

Sherwen, T., Evans, M. J., Carpenter, L. J., Andrews, S. J., Lidster, R. T., Dix, B., Koenig, T. K., Sinreich, R., Ortega, I., Volkamer, R., Saiz-Lopez, A., Prados-Roman, C., Mahajan, A. S., and Ordóñez, C.: Iodine's impact on tropospheric oxidants: a global model study in GEOS-Chem, Atmos. Chem. Phys., 16, 1161–1186, https://doi.org/10.5194/acp-16-1161-2016, 2016.

Sherwen, T., Chance, R. J., Tinel, L., Ellis, D., Evans, M. J., and Carpenter, L. J.: A machine-learning-based global sea-surface iodide distribution, Earth Syst. Sci. Data, 11, 1239–1262, https://doi.org/10.5194/essd-11-1239-2019, 2019.

Smith, S. D.: Wind stress and heat flux over the ocean in gale force winds, J. Phys. Oceanogr., 10, 709–726, 1980.

Soloviev, A. and Lukas, R.: The Near-Surface Layer of the Ocean: Structure, Dynamics and Applications, 2nd Edition, Atmos. Oceanogr. Sci. Libr., 48, 552, https://doi.org/10.1007/978-94-007-7621-0, 2014.

Sommariva, R., Bloss, W., and von Glasow, R.: Uncertainties in gas-phase atmospheric iodine chemistry, Atmos. Environ., 57, 219–232, https://doi.org/10.1016/j.atmosenv.2012.04.032, 2012.

Takashima, H., Kanaya, Y., Kato, S., Friedrich, M. M., Van Roozendael, M., Taketani, F., Miyakawa, T., Komazaki, Y., Cuevas, C. A., Saiz-Lopez, A., and Sekiya, T.: Full latitudinal marine atmospheric measurements of iodine monoxide, Atmos. Chem. Phys., 22, 4005–4018, https://doi.org/10.5194/acp-22-4005-2022, 2022.

Tham, Y. J., He, X.-C., Li, Q., Cuevas, C. A., Shen, J., Kalliokoski, J., Yan, C., Iyer, S., Lehmusjärvi, T., Jang, S., Thakur, R. C., Beck, L., Kemppainen, D., Olin, M., Sarnela, N., Mikkilä, J., Hakala, J., Marbouti, M., Yao, L., Li, H., Huang, W., Wang, Y., Wimmer, D., Zha, Q., Virkanen, J., Spain, T. G., O'Doherty, S., Jokinen, T., Bianchi, F., Petäjä, T., Worsnop, D. R., Mauldin, R. L., Ovadnevaite, J., Ceburnis, D., Maier, N. M., Kulmala, M., O'Dowd, C., Maso, M. D., Saiz-Lopez, A., and Sipilä, M.: Direct field evidence of autocatalytic iodine release from atmospheric aerosol, P. Natl. Acad. Sci. USA, 118, e2009951118, https://doi.org/10.1073/pnas.2009951118, 2021.

Tinel, L., Adams, T. J., Hollis, L. D. J., Bridger, A. J. M., Chance, R. J., Ward, M. W., Ball, S. M., and Carpenter, L. J.: Influence of the Sea Surface Microlayer on Oceanic Iodine Emissions, Environ. Sci. Technol., 54, 13228–13237, https://doi.org/10.1021/acs.est.0c02736, 2020.

Truesdale, V. W. and Jones, K.: Steady-state mixing of iodine in shelf seas off the British Isles, Cont. Shelf Res., 20, 1889–1905, https://doi.org/10.1016/S0278-4343(00)00050-9, 2000.

Tsilingiris, P.: Thermophysical and transport properties of humid air at temperature range between 0 and 100 °C, Energ. Convers. Manage., 49, 1098–1110, https://doi.org/10.1016/j.enconman.2007.09.015, 2008.

Virtanen, P., Gommers, R., Oliphant, T. E., Haberland, M., Reddy, T., Cournapeau, D., Burovski, E., Peterson, P., Weckesser, W., Bright, J., van der Walt, S. J., Brett, M., Wilson, J., Millman, K. J., Mayorov, N., Nelson, A. R. J., Jones, E., Kern, R., Larson, E., Carey, C. J., Polat, İ., Feng, Y., Moore, E. W., VanderPlas, J., Laxalde, D., Perktold, J., Cimrman, R., Henriksen, I., Quintero, E. A., Harris, C. R., Archibald, A. M., Ribeiro, A. H., Pedregosa, F., van Mulbregt, P., and SciPy 1.0 Contributors: SciPy 1.0: Fundamental Algorithms for Scientific Computing in Python, Nat. Meth., 17, 261–272, https://doi.org/10.1038/s41592-019-0686-2, 2020.

Vogt, R., Sander, R., von Glasow, R., and Crutzen, P.: Iodine Chemistry and its Role in Halogen Activation and Ozone Loss in the Marine Boundary Layer: A Model Study, J. Atmos. Chem., 32, 375–395, https://doi.org/10.1023/A:1006179901037, 1999.

Wadley, M. R., Stevens, D. P., Jickells, T. D., Hughes, C., Chance, R., Hepach, H., Tinel, L., and Carpenter, L. J.: A Global Model for Iodine Speciation in the Upper Ocean, Global Biogeochem. Cy., 34, e2019GB006467, https://doi.org/10.1029/2019GB006467, 2020.

Wang, T. X. and Margerum, D. W.: Kinetics of reversible chlorine hydrolysis: Temperature-dependence and general acid/base assisted mechanisms, Inorg. Chem., 33, 1050–1055, https://doi.org/10.1021/ic00084a014, 1994.

Wang, T. X., Kelley, M. D., Cooper, J. N., Beckwith, R. C., and Margerum, D. W.: Equilibrium, kinetic and UV-spectral characteristics of aqueous bromine chloride, bromine and chlorine species, Inorg. Chem., 33, 5872–5878, https://doi.org/10.1021/ic00103a040, 1994.

Wang, X., Jacob, D. J., Downs, W., Zhai, S., Zhu, L., Shah, V., Holmes, C. D., Sherwen, T., Alexander, B., Evans, M. J., Eastham, S. D., Neuman, J. A., Veres, P. R., Koenig, T. K., Volkamer, R., Huey, L. G., Bannan, T. J., Percival, C. J., Lee, B. H., and Thornton, J. A.: Global tropospheric halogen (Cl, Br, I) chemistry and its impact on oxidants, Atmos. Chem. Phys., 21, 13973–13996, https://doi.org/10.5194/acp-21-13973-2021, 2021.

Wang, Y. L., Nagy, J. C., and Margerum, D.: Kinetics of hydrolysis of iodine monochloride measured by the pulsed-accelerated-flow method, J. Am. Chem. Soc., 111, 7838–7844, https://doi.org/10.1021/ja00202a026, 1989.

Wesely, M. and Hicks, B.: Some Factors that Affect the Deposition Rates of Sulfur Dioxide and Similar Gases on Vegetation, J. Air Pollut. Contr. Assoc., 27, 1110–1116, https://doi.org/10.1080/00022470.1977.10470534, 1977.

Wurl, O., Wurl, E., Miller, L., Johnson, K., and Vagle, S.: Formation and global distribution of sea-surface microlayers, Biogeosciences, 8, 121–135, https://doi.org/10.5194/bg-8-121-2011, 2011.

Wurl, O., Ekau, W., Landing, W. M., and Zappa, C. J.: Sea surface microlayer in a changing ocean – A perspective, Elementa, 5, 31, https://doi.org/10.1525/elementa.228, 2017.

Xiong, H., Lee, J., Zare, R., and Min, W.: Strong Electric Field Observed at the Interface of Aqueous Microdroplets, J. Phys. Chem. Lett., 11, 7423–7428, https://doi.org/10.1021/acs.jpclett.0c02061, 2020.

Young, P. J., Archibald, A. T., Bowman, K. W., Lamarque, J.-F., Naik, V., Stevenson, D. S., Tilmes, S., Voulgarakis, A., Wild, O., Bergmann, D., Cameron-Smith, P., Cionni, I., Collins, W. J., Dalsøren, S B., Doherty, R. M., Eyring, V., Faluvegi, G., Horowitz, L. W., Josse, B., Lee, Y. H., MacKenzie, I A., Nagashima, T., Plummer, D. A., Righi, M., Rumbold, S. T., Skeie, R. B., Shindell, D. T., Strode, S. A., Sudo, K., Szopa, S., and Zeng, G.: Preindustrial to end 21st century projections of tropospheric ozone from the Atmospheric Chemistry and Climate Model Intercomparison Project (ACCMIP), Atmos. Chem. Phys., 13, 2063–2090, https://doi.org/10.5194/acp-13-2063-2013, 2013.